

Characterization and interpretation of the global lunar impact basins based on remote sensing

Jingwen Liu^{a,b,c}, Jianzhong Liu^{a,c,*}, Zongyu Yue^{c,d}, Li Zhang^{a,c}, Juntao Wang^{a,c}, Kai Zhu^{a,c}

^a Center for Lunar and Planetary Sciences, Institute of Geochemistry, Chinese Academy of Sciences, Guiyang 550081, China

^b University of Chinese Academy of Sciences, Beijing 100049, China

^c Center for Excellence in comparative planetology, Chinese Academy of Sciences, Hefei 230026, China

^d State Key Laboratory of Remote Sensing Science, Aerospace Information Research Institute, Chinese Academy of Sciences, Beijing 100101, China

ARTICLE INFO

Keywords:

Moon
Impact basins
Basin sub-formation
Global basin map
Focal flow data

ABSTRACT

Impact basins are primary geological structures on the Moon, and play key roles in revealing the lunar history. Due to the different identification standards currently used, the basin identification results are highly inconsistent. Except for the major basins (e.g., Orientale, Schrödinger, Imbrium, Crisium, Apollo, and Nectaris Basin), detailed sub-formation interpretations for most other basins are lacking, which hampers the construction of a complete (global) geological interpretation for the lunar impact basins. Based on multisource remote sensing data and previous works, we established a basin identification standard, and a new global lunar basin catalog containing 81 basins. According to the ring diameter ratios, the purest anorthosite (PAN) distribution, and basin radial textures, we divided the basin sub-formations into the central-peak, peak-ring, basin-floor, basin-wall, basin-rim, and basin-ejecta formations. We interpreted the ejecta formation and other basin sub-formations by combining the Focal Flow data with LROC WAC images, topographic data, gravity anomalies, and spectral data. Our new lunar geologic map shows more precise distribution of basin formations, covering nearly 70% of the lunar surface. Moreover, we obtained the origin of basin rings using basin sub-formations map. Additionally, the basin sub-formation map can contribute to the basin impact conditions, such as the discovered ring (concentric with the outermost ring) provides evidence for three impacts in the Mare Moscoviense, and the SPA sub-formation distribution indicates the impact direction of SPA is SE-NW. Furthermore, the sub-formation distribution can facilitate the geological characteristics and evolution study of the lunar exploration sites.

1. Introduction

Lunar impact basins are massive impact structures (Le Feuvre and Wieczorek, 2011) and have a major influence on the lunar stratigraphy, tectonics, and crustal structure (Spudis, 1993). Basin impact events are important in the lunar evolution, as they recorded the history of impactors in the early solar system. However, as the identification criteria are not uniform, the identification results vary widely (Wilhelms et al., 1987; Wood, 2004; Neumann et al., 2015; Byrne, 2016). Before the GRAIL mission was launched, impact features of >300 km (diameter) were regarded as impact basins (Wilhelms et al., 1987). However, most craters >200 km (rim-to-rim diameter) are now regarded as impact basins based on GRAIL data analysis (Miljković et al., 2013; Neumann et al., 2015). When the basin diameter is <200 km, most of the impact energy (imparted by shock wave) is converted to the kinetic energy of

the ejecta, whereas an increasing proportion of that energy is converted to material melting/vaporization if the basin diameter goes above 200 km (Miljković et al., 2013). Meanwhile, the gravity and terrain characteristics of the impact structure are easily confused with those of some sizeable lunar basalt filling areas (e.g., Mare Frigoris; Wood, 2004) and volcanic craters (e.g., Grissom-White; Wilhelms et al., 1987; Wood, 2004; Losiak et al., 2015). In this study, therefore, we established a set of basin identification standards and a new global lunar basin catalog (with 81 basins) based on multisource remote sensing data and previous studies.

Basin geological units are one of the primary elements in lunar geological mapping. Delineating the geological structures in large lunar basins is essential to understand the origin of basin rings, the transient cavity volume, the original sampling depth, and the nature of the basin formation processes (Fassett et al., 2011). Basin ejecta provides

* Corresponding author at: No. 99 West Lincheng Road, Guanshanhu District, Guiyang, Guizhou Province 550081, China.

E-mail address: liujianzhong@mail.gyig.ac.cn (J. Liu).

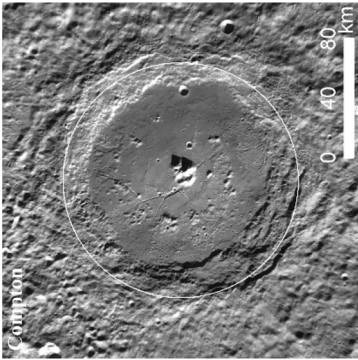
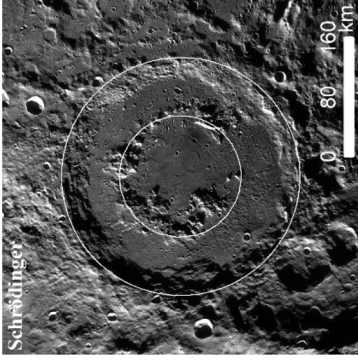
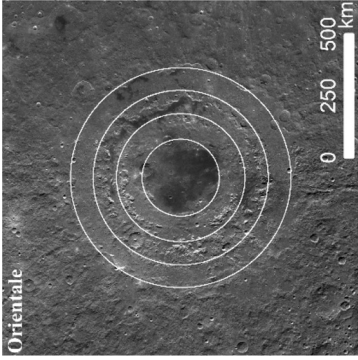
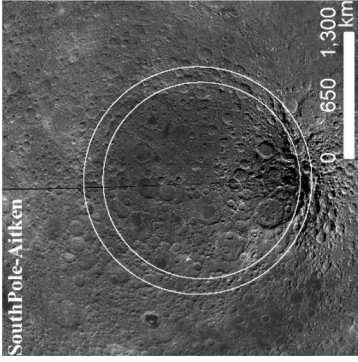
<https://doi.org/10.1016/j.icarus.2022.114952>

Received 13 February 2021; Received in revised form 12 February 2022; Accepted 15 February 2022

Available online 22 February 2022

0019-1035/© 2022 Published by Elsevier Inc.

Table 1
The identity standard of the four types of basins focused on morphology, deep structure, and impact mechanism.*

	Proto Basin	Peak Ring Basin	Multi-ring Basin	Super Basin
Morphology				
Central Peak	Open clusters of central peaks are unusually small or even absent if they are enough old.			
Rings structure	the arc <math>< 180^\circ</math>	the arc angle >math>> 180^\circ</math>	n (rings) > 3	The ring is much larger than others
Bouguer anomaly(BA)	r (Positive BA) < r(peak ring)	r (positive BA) \approx r(peak ring) r (negative BA) \approx r(rim)	Each ring has a gravity anomaly with alternating positive and negative	The positive BA in the center; falls off to 0 at the rim
Formation mechanism	mantle uplift appear	mantle uplift and basalt filling	mantle uplift and basalt filling	The impact target as a sphere rather than a plane or an arc

* The white circles in LROC WAC data images represent the topographic rings of impact basins

information on the lunar time-stratigraphy. Orientale Basin ejecta (Hevelius Formation) is the dating section of the early and late Imbrian period, Imbrium Basin ejecta (Fra Mauro Formation) is the dating section of the Imbrian period and Nectarian Period, Nectaris Basin ejecta (Jassen Formation) is the dating section of Nectarian and Aitkenian periods (Wilhelms et al., 1987; Guo et al., 2014). Basin sub-formations cover almost all of the lunar surface and are the direct objects of the lunar exploration projects. Analysis of the basin morphology and geological formations can provide valuable information to facilitate scientific research projects. A better understanding of the basin geological units can also provide insight into the lunar history and composition, as well as clues for future lunar exploration.

Major lunar basins (e.g., Orientale, Schrödinger, Imbrium, Crisium, Apollo, and Nectaris) have been thoroughly analyzed by previous studies (Spudis et al., 2014; Chen et al., 2014; Steenstra et al., 2016; Wu et al., 2018; Sliz and Spudis, 2016; Potter et al., 2018; Morse et al., 2018). However, the expression of the geological units about these basins is inconsistent. Lithology and morphological descriptions are used interchangeably, or descriptions involve regional proper nouns (Maunder, Fra Mauro, et al), which cannot be applied to the analysis of the global basin geological units. In March 2020, the United States Geological Survey (USGS) has published the first standardized 1:5 M lunar geologic map (Fortezzo et al., 2020). But there are some disadvantages: (1) The classification of basin geologic units is chaotic, including Basin Lineated, Basin Massif, Basin Secondary Crater, and Imbrium, Orientale, Nectaris sub formations. (2) The basin geological unit and other non-basin geological units are mixed on the same layer, showing a patchy distribution. (3) Geological unit information is lacking in many basins, especially the basins newly detected by GRAIL data. The absence of the global geologic basin map limited the research on the lunar geologic history.

The term “formation” refers to the fundamental unit in lithostratigraphic classification and can be subdivided (Salvador, 1994), and has appeared in the description of lunar basin geological units. For example, the Hevelius, Montes Rook, and Maunder formations in the Orientale Basin constitute the Orientale Group (Wilhelms et al., 1987). This study aims to interpret the geological unit that matches the basin ring structures through the formation. However, it is unrealistic to name different basin sub-formations with related names nearby. Consequently, a unified sub-formation classification system is established, combining the impact crater subdivided theory and basinal structures. This classification is more helpful for comprehensive basin analysis and research, e.g., the origin of basin rings, transient cavity volume, original sampling depth, and basin-forming processes.

After over a half-century of work, there is currently some consensus on the formation of impact basin rings on the Moon and terrestrial planets (Hartmann and Kuiper, 1962; Hartmann and Wood, 1971; Pike and Spudis, 1987; Melosh, 1989; Spudis, 1993; Alexopoulos and McKinnon, 1994; Head 3rd et al., 2010; Baker et al., 2011a, 2011b). On most rocky planetary bodies, the onset of basin formation occurs when central peaks within complex craters are replaced by an interior ring of peaks to form peak-ring basins (Hartmann and Wood, 1971; Head, 1977; Pike and Spudis, 1987; Baker et al., 2011a, 2011b). Transitional crater forms, called proto-basins, possessing both central peaks and peak rings are also observed (Pike and Spudis, 1987; Baker et al., 2011a, 2011b). At the largest basin sizes, additional rings are added to form multi-ring basins (Head, 1977; Potter, 2015).

A series of basinal features is derived through the remote sensing data from the recent lunar missions (e.g., LOLA, GRAIL, Kaguya, Chandrayaan-1, CE-1, CE-2, CE-3, and CE-4). A global impact basin map covering 70% of the lunar surface is established.

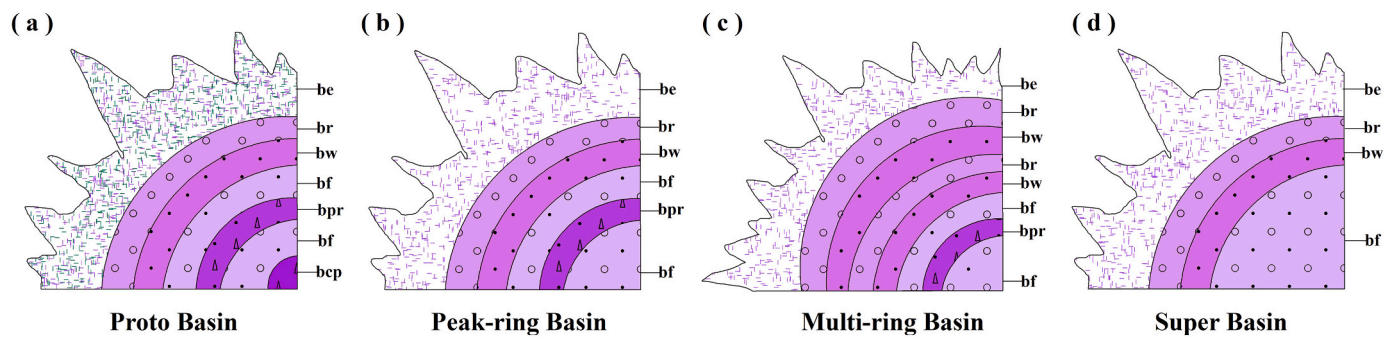


Fig. 1. Basin formation named by facies belt. (a). the basin sub-formations of Proto-Basin from inner to outer: Central peak formation(bcp), Basin floor formation(bf), Peak ring formation(bpr), Basin floor formation(bf), Basin wall formation(bw), Basin rim formation(br), Basin Ejecta formation(be); (b) the basin sub-formations of Peak-ring Basin inner to outer: Basin floor formation(bf), Peak ring formation(bpr), Basin floor formation(bf), Basin wall formation(bw), Basin rim formation(br), Basin Ejecta formation(be); (c) the basin sub-formations of Multi-ring Basin inner to outer: Basin floor formation(bf), Peak ring formation(bpr), Basin floor formation(bf), Basin wall formation(bw), Basin rim formation(br), Basin wall formation(bw), Basin rim formation(br), Basin Ejecta formation(be); (d) the basin sub-formations of Super Basin from inner to outer: Central peak formation(bcp), Basin floor formation(bf), Peak ring formation(bpr), Basin floor formation(bf), Basin wall formation(bw), Basin rim formation(br), Basin Ejecta formation(be).

2. Datasets and methods

2.1. Datasets

To interpret the basin formations, multi-source high-resolution lunar data were compiled, including (1) high-resolution Lunar Reconnaissance Orbiter (LRO) wide-angle camera (LROC WAC) images (118 m/pixel resolution) (Robinson et al., 2010). A mosaic of LROC WAC images forms the first basis for our photogeological study; (2) Lunar Orbiter Laser Altimeter (LOLA) onboard LRO topographic data (118 m/pixel resolution) (Smith et al., 2010). LOLA data can be used to determine the slope of the lunar surface, analyzing which is essential to locate the transitional zones between different geological units, notably basal wall and rim; (3) Global distribution maps of FeO and TiO₂ (Pieters et al., 1994; Lucey et al., 1998) based on Clementine mission spectral data. These data were used to assess the unit boundaries defined based on their morphological characteristics; (4) High-resolution (better than 15 km/pixel) lunar gravity field model GRGM900C from the GRAIL mission (Zuber et al., 2013) and gravity gradient data (Andrews-Hanna et al., 2018). We used these data to assess severely-degraded impact basins; (5) 1:5 M USGS lunar geologic map (Fortezzo et al., 2020) and published geologic maps of individual basins (e.g., Orientale, Schrödinger, Imbrium, Crisium, Apollo, and Nectaris) (Spudis et al., 2014; Chen et al., 2014; Steenstra et al., 2016; Wu et al., 2018; Sliz and Spudis, 2016; Potter et al., 2018; Morse et al., 2018) are used as a reference in vectoring basin geological units.

2.2. Identification features of impact basins

Five primary lunar basin databases, i.e., those by Wilhelms et al. (1987) (45 basins), Wood (2004) (58 basins), Neumann et al. (2015a) (74 basins), Byrne (2016) (72 basins), and the Lunar Impact Crater Database (64 basins, including only those with >200 km rim-to-rim diameter) (Losiak et al., 2015) are analyzed here. These five databases contain 108 considered impact basins, and only 30 basins appear simultaneously in all of the five databases. The identification features of impact basins are given in combination with the characteristics of the 30 basins in multi-remote sensing data and the impact mechanism in this paper. Impact basins have two classical impact structures: (1) although the basin ejecta would disappear with degradation, the ejecta are almost entirely destroyed by later destructive impact events, and the terrain boundary has become diffused, the deep radial structures can still be found in the gravity gradient and DEM data; (2) as these basins are large, arc-shape traces are still preserved after a long time in all remote sensing data.

Although the ring characteristics will be retained, the morphology of the ring characteristics of different basins has certain differences. Our new work and previous studies (Hartmann and Kuiper, 1962; Melosh, 1989; Baker et al., 2012; Osinski, 2012) suggest that lunar basins fall into four major types (i.e., proto, peak-ring, multi-ring, and super basins that refers to the SPA in Table 1), based on their morphology, deep structure, and impact mechanism. The characteristics of each type are as below:

Proto-Basin. (1) These basins have open clusters of central peaks, and they are usually larger than tight peaks clusters in central peak craters. The basin central mountains are unusually small or even absent if they are enough old. (2) These basins' central peak rings are systematically smaller than those of peak ring basins. (3) Some older ones have a positive Bouguer anomaly in the center although the width is small. (4) Compared with complex impact craters, there is a mantle uplift in the proto-basin and this is the essential difference between a crater and a basin (Baker et al., 2011a, 2011b).

Peak-ring basins. (1) These basins have roughly circular rings although sometimes discontinuous. (2) These basins have a central positive Bouguer anomaly that is confined within the peak ring and a negative Bouguer anomaly annulus that extends from the edge of the positive anomaly outward to the rim crest (Baker et al., 2017). (3) The lunar mantle uplift is more pronounced than the proto-basin.

Multi-ring basins. (1) These basins have more than three rings. (2) Each ring of them has a Bouguer anomaly. The size of the central Bouguer anomaly is comparable with the diameters of the innermost topographic rings of Multi-ring basins (Neumann et al., 2015). (3) They have obvious mantle uplift and basalt filling.

Super Basin. It mainly refers to the SPA. The morphology is very large, and the impact mechanism is unique. (1) The basin diameter almost coincides with the lunar diameter, and the structure is large enough to be classified as one of the three major lunar terranes (Jolliff et al., 2000). (2) The ring ratio of SPA is much smaller than other basins. (3) The formation mechanism is different from other basins, and the impact target must be treated as a sphere rather than a plane or an arc.

2.3. Classification and interpretation of basin sub-formations

2.3.1. Basin geological units based on facies belts

An accepted geological division in mapping impact craters (from center to rim) is as follows: central peak, crater floor, crater walls (Wilhelms et al., 1987). Although many impact basins are structurally much more complex than a crater, they can share the same geological division scheme (Wilhelms et al., 1987). Combined with the ring diameter ratios (section 4.1), the purest anorthosite (PAN) distribution

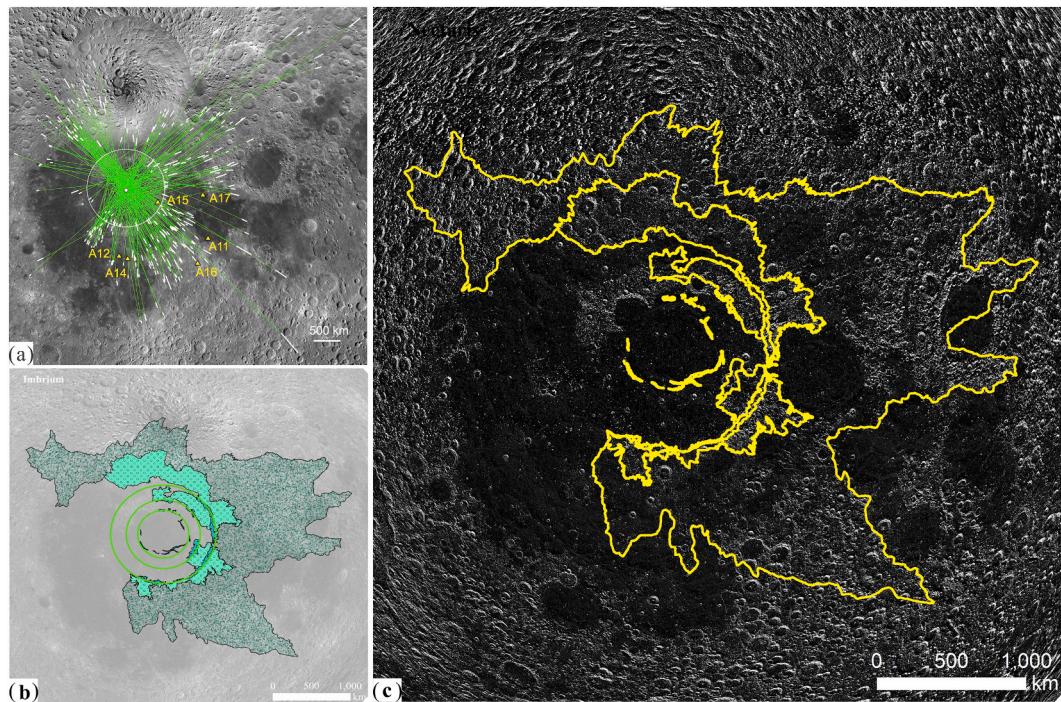


Fig. 2. (a) all grooves and secondary craters on the Imbrium Basin centered map in a Lambert-stereographic conformal projection centered on Imbrium (offset from the center here) Schultz and David (2016); (b) Imbrium basin formations geologic map in a Lambert-Azimuthal-Equal-Area projection centered on Imbrium (offset 0, 0); (c) Imbrium basin formations edges (yellow line) layered with focused stream data in a Lambert-Azimuthal-Equal-Area projection centered on Imbrium (offset 0, 0).

(section 4.1), and basin radial texture (section 4.2), basin formation named by facies belt in each type of basin is consistent with its ring structures (Fig. 1). The sub-formations include six types. (1) Central peak formation (bcp): Mountains are distributed in clusters in the proto-basin center. The slope and roughness values are very high in the central-peak formation; (2) Peak-ring formation (bp): Mountains are distributed in groups and form a ring structure in the center of the peak-ring basins and proto-basins, which divided the basin floor into two parts. The slope and roughness values are high; (3) Basin-floor formation (bf): The basin center is flat and low; (4) Basin-wall formation (bw): The area outside the basin varies from low to high. The slope is much steeper than that in the other five formations; (5) Basin-rim formation (br): Ejecta blanket, elevation is higher than the pre-impact crust; (6) Basin-ejecta formation (be): linear structures and the secondary craters are radially distributed outside the basins. The elevation is the same as the pre-impact crust.

2.3.2. Basin sub-formations

Using geographic information system software GIS, we created point (basin coordinate spots), line (basin ring structures), and polygon (basin formations) shapefiles of each basin of the new catalog in a Lambert-Azimuthal-Equal-Area projection centered on the basin. The background data are sequentially layered as below: LROC WAC images (0% transparency), the ColorShade image of LOLA (50% transparency), GRGM900C, gravity gradients, FeO and TiO₂ distributions, LOLA, LOLA slope, dem roughness map, and geo-registered geological maps of in 1:5 M USGS lunar geologic map (e.g., Orientale, Schrödinger, Imbrium, Crisium, Apollo, Moscovlense, Medii, Humor, Mendeleev, Birkhoff, Keeler West, Miline, Poincare, and Humboldtianum) (Fortezzo et al., 2020) and in the literature (e.g., Orientale, Schrödinger, Imbrium, Crisium, Apollo, and Nectaris) (Spudis et al., 2014; Chen et al., 2014; Steenstra et al., 2016; Wu et al., 2018; Sliz and Spudis, 2016; Potter et al., 2018; Morse et al., 2018). The basin profile features can be revealed by continuously adjusting the display colour label, transparency, contrast degree of these remote sensing data. We determined

the basin type and used the editor tool in the GIS software to mark the center and ring structures of the basins. The type of basin sub-formations was determined by combining the ring-structure features of different basin types. The borderlines of basin sub-formations are vectorized based on the layered data. The interpreted examples of the proto-basin (Fig. S3), peak-ring basin (Fig. S4), and multi-ring basin (Fig. S5) are shown.

This interpretation of the basin sub-formations, especially the multi-ring basin is more detailed than previous studies (Spudis et al., 2014; Chen et al., 2014; Steenstra et al., 2016; Wu et al., 2018; Sliz and Spudis, 2016; Potter et al., 2018; Morse et al., 2018; Fortezzo et al., 2020). As shown in Fig. S5, the Orientale Basin contains the Hevelius, Montes Rook, and Maunder formations in previous works (Potter et al., 2018; Morse et al., 2018; Fortezzo et al., 2020). Sub-formations of Orientale Basin are consistent with ring structure here, including (from the center outward) the basin-floor, peak-ring, basin-floor, basin-wall, basin-rim, and basin-ejecta formations.

2.3.3. Focal flow spatial analysis

As we have known, the majority of the ejecta material is fluidized and able to flow in accordance with local topography, especially in the case of impact basins with large impact scales. As a result, deep tracking of DEM data can identify ejecta information. To improve the ejecta range and vectorized the resolution of the sub-formations, the Focal Flow spatial analysis is adopted (Fig. 2c), which is a neighborhood analysis method to determine the flow of the values in the input raster within the immediate neighborhood of each cell (Morio et al., 2010). In this study, the Focal Flow analysis eliminates the interference of small fluctuations, and reveals macro-scale terrain variation trends. The yellow boundary lines in Fig. 2c (based on the Focal Flow LOLA data) are mostly consistent with the density distribution of secondary craters and radiation textures drawn (LROC WAC -based) by Schultz and Crawford (2016) (Fig. 2a). As the local topographic highs and lows have a significant impact on the flow direction and distance of ejecta material despite the initial outward momentum imparted by the impact, no ejecta

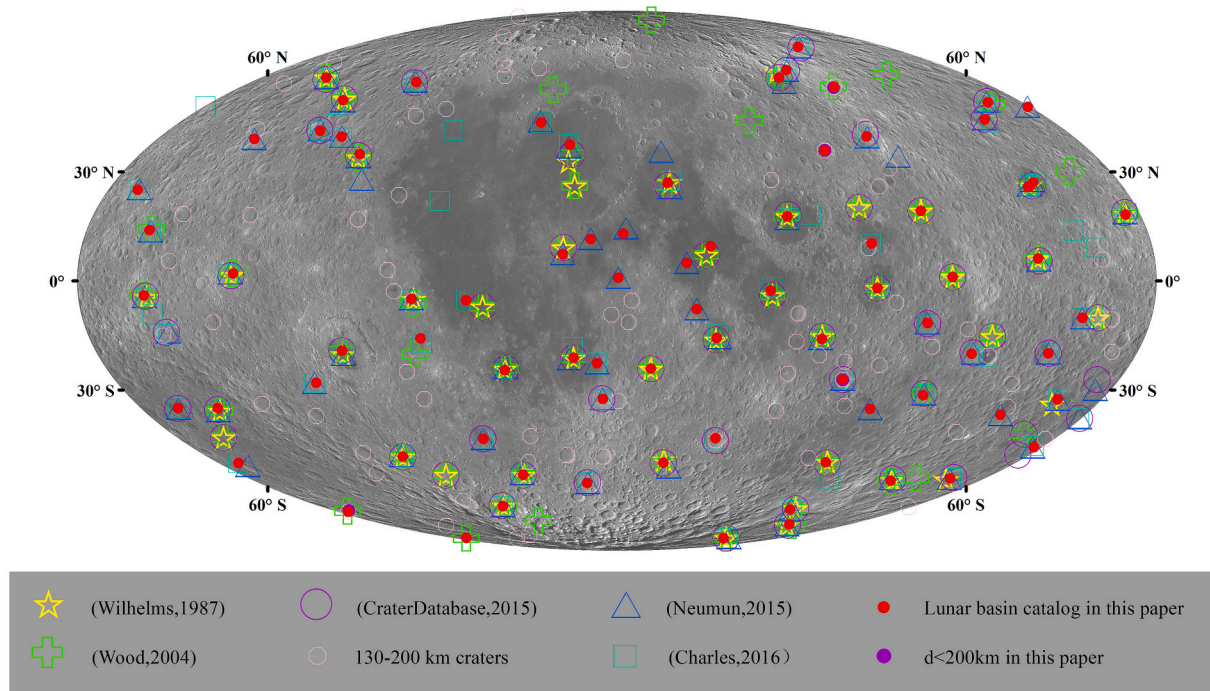


Fig. 3. New lunar basin catalog. The Map is shown using a Mollweide equal-area projection, centered over the lunar farside at 180° E, 0° N. The yellow stars represent the basins of [Wilhelms et al. \(1987\)](#); the green crosses represent the basins of [Wood \(2004\)](#); the purple circles represent the crater which diameter larger than 200 km in ([Losiak et al., 2015](#)); the yellow pentagons represent the crater which diameter in 130 km–200 km in ([Losiak et al., 2015](#)); the blue triangles represent the basins of [Neumann et al. \(2015\)](#); the cyan squares represent the basins of [Byrne \(2016\)](#); the red dots represent basins in our new lunar basin catalog; the purple dots represent the proto-basins in our new lunar basin catalog. (For interpretation of the references to colour in this figure legend, the reader is referred to the web version of this article.)

was identified in the southwest of the Imbrium Basin in our result and other researches ([Fig. 2c](#)).

At the same time, since the traditional ejecta identification method involves finding the secondary crater, impact crater clusters, radial linear structures, etc. in image data, DEM data, the recognized sputter information is the linear discontinuous. This method in our article can find the radiant ejecta information similar to the radiation pattern in the Copernican craters, which is more conducive to the drawing of the ejecta boundary in the geological map of the Moon.

Based on the Focal Flow data, the basin ejecta formations in the Imbrian and Nectarian periods and the basin rim formations (continuous sputter blanket) in the Aikenian period are identified. More comparison with other mapping techniques is can be seen in the interpretation results of the Orientale Southwest Basin in chapter 4.2.1.

3. Results

3.1. New basin catalog

There are 80 impact structures in the five published databases mentioned above that are identified as impact basins including 30 common basins, and 28 basins are excluded by the impact basin identification criteria proposed in this study. These basins fall into four major types: (1) Geologic structures that are too large, not recognized as impact basins by most scholars, such as the Nearside Megabasin ([Byrne, 2016](#)) and Procellarum ([Wilhelms et al., 1987](#); [Wood, 2004](#)); (2) filled with basalt with a volcanic origin, e.g., eastern Mare Frigoris ([Wood, 2004](#)), west of Atlas ([Wood, 2004](#)), east of Mare Humboldtianum ([Wood, 2004](#)), Sylvester-Nansen ([Wood, 2004](#)), Grissom-White, Keeler-Heaviside, Tsiolkovsky- Stark ([Wilhelms et al., 1987](#); [Wood, 2004](#); [Losiak et al., 2015](#)), near the crater Darwin ([Wood, 2004](#)), Bailly-Newton ([Wood, 2004](#)), and Pingre-Hausen ([Wilhelms et al., 1987](#);

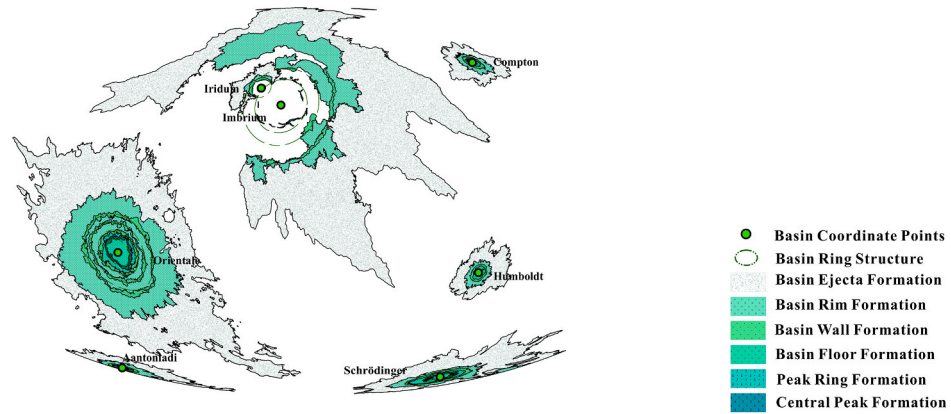
[Wood, 2004](#)), Crisium East ([Byrne, 2016](#); [Neumann et al., 2015a](#)), Insularum ([Wilhelms et al., 1987](#); [Wood, 2004](#); [Losiak et al., 2015](#)); (3) Central peak impact craters, such as Tsiolkovskiy ([Byrne, 2016](#)), Galois ([Byrne, 2016](#); [Neumann et al., 2015](#); [Losiak et al., 2015](#)), Leibnitz ([Byrne, 2016](#); [Neumann et al., 2015](#); [Losiak et al., 2015](#)), Van de Graaff ([Losiak et al., 2015](#)); (4) other types, such as Jeans-Priestly ([Byrne, 2016](#)) (only with broken arc-shape, basalt-filled), Kohlschutter-Leonov ([Byrne, 2016](#)) (only with broken arc-shape), Lavoisier-Mairan ([Byrne, 2016](#)) (only with broken arc-shape, basalt-filled), Cardanus-Herodotus ([Byrne, 2016](#)) (mostly basalt-filled), Szilard North ([Neumann et al., 2015](#)) (just a crater of 120 km diameter not a basin), Champlygin-Mandel ([Byrne, 2016](#)) (only a tiny crater of 95 km diameter not a basin), Bartels-Voskresenskiynearly ([Neumann et al., 2015](#)) (only a tiny crater of 139 km diameter not a basin), nearly coincident with crater D'Alembert and north of Mare Moscoviense ([Wood, 2004](#)) (serious degradation, no obvious impact feature in gravity and DEM data), Serenitatis North ([Neumann et al., 2015](#)) (only gravitational anomalies, no other impact features).

The Antoniadi, Compton, and Humboldt craters are below 200 km in diameter but were regarded as basins in earlier studies ([Hodges and Wilhelms, 1978](#); [Pike and Spudis, 1987](#); [Baker et al., 2011a, 2011b](#)). [Hawke and Head \(1977\)](#) proposed that the 130 km in diameter is the lower limit appearing the basin characteristics. We identified 72 impact structures (130–200 km diameter) using multi-source data and classified the four craters (i.e., Humboldt, Compton, Antoniadi, and Gauss) with <200 km rim-rim diameter as impact basins. Finally, a basin catalog that contains 81 impact basins was built in this paper ([Fig. 3](#); [Table S1](#)).

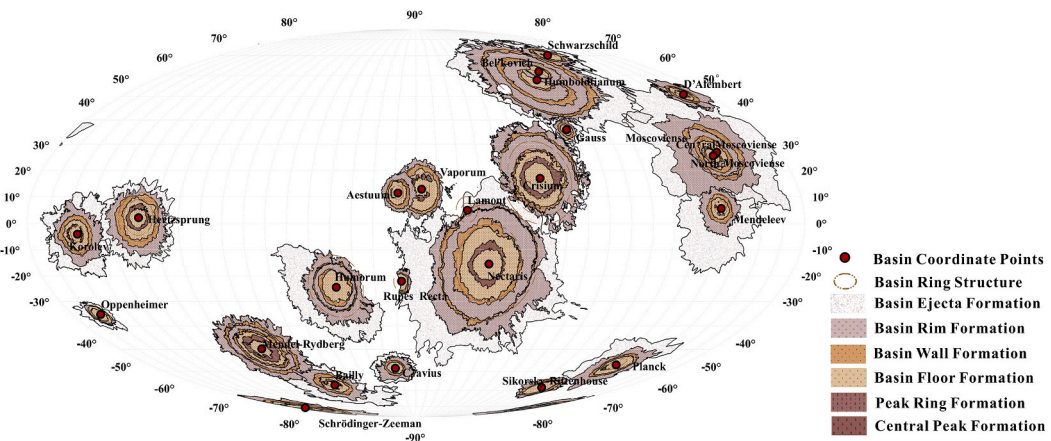
3.2. Map of impact basin formation

This paper has divided the 81 impact basins into three age periods based on previous studies, i.e., Imbrian, Nectarian, and Aitkenian

(a) Global lunar impact basins geologic map in Imbrian Period



(b) Global lunar impact basins geologic map in Nectarian Period



(c) Global lunar impact basins geologic map in Aitkenian Period

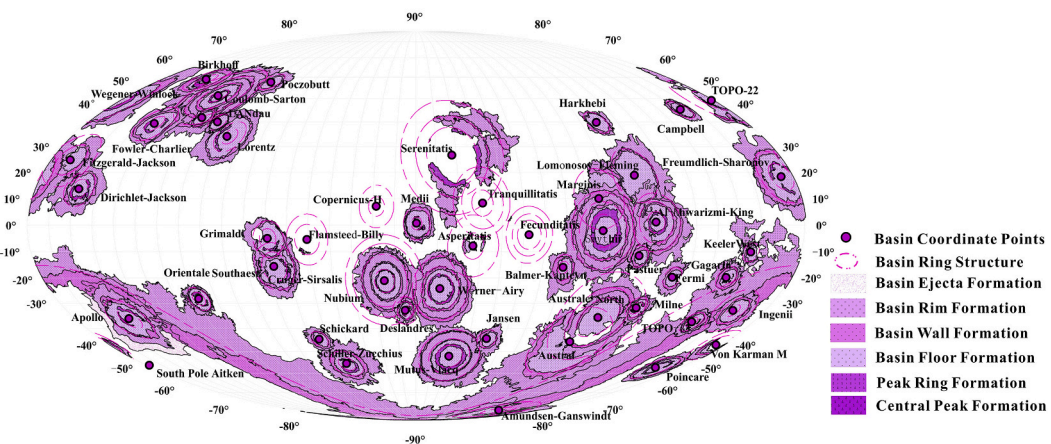


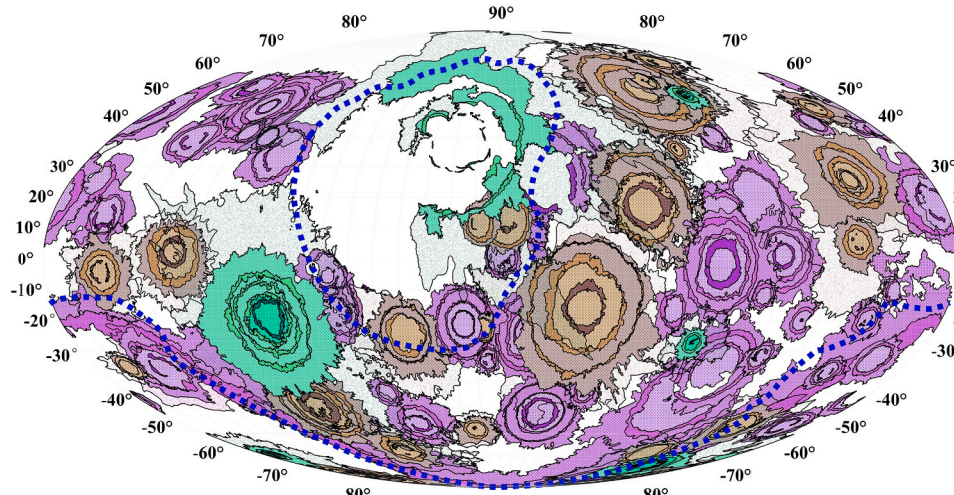
Fig. 4. Impact basins' spatial information (The Map is shown using a Mollweide equal-area projection, centered at 180° E, 0° N). (a) Global lunar impact basins geologic map in Imbrian Period; (b) Global lunar impact basins geologic map in Nectarian Period; (c) Global lunar impact basins geologic map in Aitkenian Period.

(Wilhelms et al., 1987; Wood, 2004; Neumann et al., 2015; Byrne, 2016; Conrad et al., 2018). This study focuses on the distribution of geological units. Thus, their morphologic centers (image and DEM data center coordinate) are more suitable as central coordinates than other centers (GRAIL or Spectral data coordinate) (Table S1; Fig. 3). The ring structure features are identified (Table S1). Basin sub-formations are mapped (Fig. 4).

Structures of the Imbrian-aged basins are relatively well-preserved

and have sharp features and steep slopes. The ejecta texture and secondary craters within three radii distances are easily defined (Fig. 4a). Seven basins identified in this study are mainly distributed in the Procellarum KREEP Terrane (PKT) and the South Pole-Aitken Terrane (SPAT) region, as well as locally in the Feldspathic High-lands Terrane (FHT). The scale of our Imbrian-aged basins sub-formations map is 1:5000 to 1:500000. Six basin sub-formations (from the basal center outward) are recognized. Unlike other Imbrian basins, the Imbrium

(a) Global lunar impact basins geologic map layered with lunar terrains



Imbrian Basin Formations

- Basin Ejecta Formation (Ibe)
- Basin Rim Formation (Ibr)
- Basin Wall Formation (Ibw)
- Basin Floor Formation (Ibf)
- Peak Ring Formation (Ibpr)
- Central Peak Formation (Ibcpr)

Nectarian Basin Formations

- Basin Ejecta Formation (Nbe)
- Basin Rim Formation (Nbr)
- Basin Wall Formation (Nbw)
- Basin Floor Formation (Nbf)
- Peak Ring Formation (Nbpr)
- Central Peak Formation (Nbcpr)

Aitkenian Basin Formations

- Basin Ejecta Formation (Abe)
- Basin Rim Formation (Abr)
- Basin Wall Formation (Abw)
- Basin Floor Formation (Abf)
- Peak Ring Formation (Abpr)
- Central Peak Formation (Abcpr)
- Basalt
- lunar terranes outline

(b) Global lunar impact basins geologic map layered with basalts

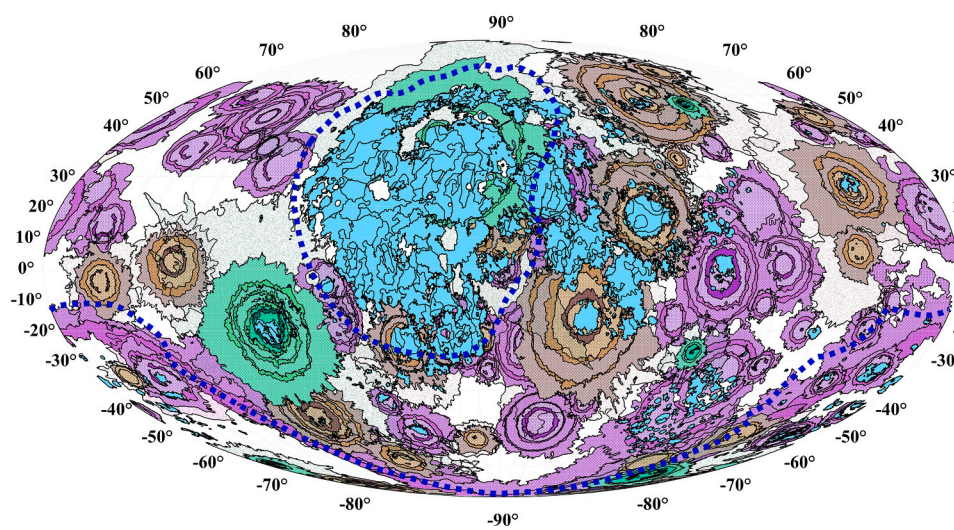


Fig. 5. Asymmetry distribution of global basin formations. (a) Global lunar impact basins geologic map layered with lunar terrains; (b) Global lunar impact basins geologic map layered with basalts.

Basin has basaltic flow covering most of its surface, and thus only parts of its formations are interpreted. We have mapped a series of floor, wall, and rim formations and obtained the ejecta distribution range. There are no traces of the Imbrium Basin ejecta in the southwest, but we found ejecta formations cover the lunar North Pole and the Nectaris and Crisium basins.

The Nectarian-aged basins are severely degraded. We have identified their central peak, peak ring, floor, wall, and rim formations and only some ejecta in half radius range have been identified. None of the 25 basins mapped in this work have been found in the northwestern part (0–90°N, 0–180°W) of the Moon (Fig. 4b). The scale of the Nectarian basin sub-formations map is from 1:10000 to 1:1000000. 15 basins' sub-formations (from the basinal center outward) are recognized. In particular, the ejecta formations of the Aestunm, Vaporum, and Crisium (near the PKT) were not found due to the basalt cover. Moreover, the ejecta of the Schrödinger-Zeeman Basin and Sikorsky-Rittenhouse Basin is covered by the formations of the Schrödinger Basin, the ejecta of Mendel-Rydberg Basin is covered by the ejecta of the Orientale Basin, and therefore we did not interpret them. Only two basins (Rupes Recta Basin, Lamont Basin) are relatively small and located near the PKT, which are severely degraded, and only ring constructions have been

identified.

The Aitkenian-aged basins are significantly degraded. Forty-nine basins have been mapped in this study (Fig. 4c). The formations of these basins can only be partly interpreted on a larger scale (1:50000 to 1:1000000) than the basin formations in the other two periods. We identified all the sub-formations of the Apollo Basin, all other basin sub-formations except the ejecta formations of 38 basins, and the outermost rims are relatively narrow. Moreover, some formations are not well mapped due to the basalt cover, degradation, and covering by younger basin formations, especially near the Orientale, Imbrium, Nectaris, Humboldtianum, and Moscoviense basins. Considering also the previous studies on ring structures (Garrick-Bethell and Zuber, 2009; Ishihara et al., 2014), we interpreted the basin wall and rim for the South Pole-Aitken Basin.

We have merged the three-period basin sub-formations maps into a global map. The map covers nearly 70% of the lunar surface (Fig. 5a), leaving out only the areas that are too degraded to be recognized. After being layered with basalt data (Hiesinger, 2003; Hiesinger et al., 2011; Pasckert et al., 2018a, 2018b), the map covers nearly 90% of the lunar surface (Fig. 5b).

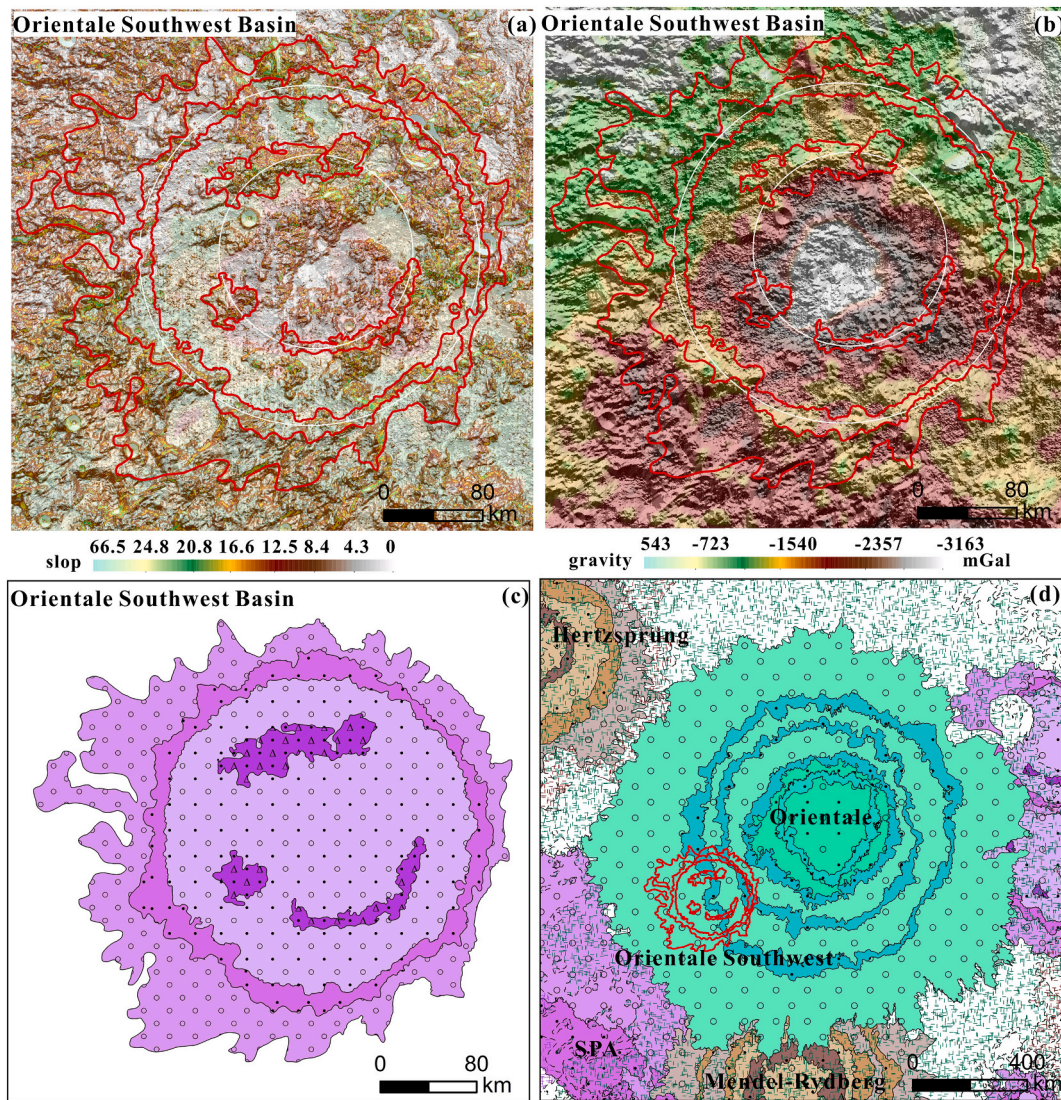


Fig. 6. The ring diameter ratio of impact basins (a) relation between peak ring diameter and the basin rim crest diameter for peak ring basin; (b) reference of peak ring diameter and the basin rim crest diameter for proto-basin; (c) relation between intermediate ring diameter and inner ring diameter for the multi-ring basin; (d) relation between outer ring diameter and the intermediate ring diameter for multi-ring basin.

4. Discussion

4.1. Basis for the basin sub-formation division

As mentioned in Section 2.3.1, there are six types of sub-formations in the four basins' types. There is no dispute on the division of central-peak, basin-floor, basin-wall, and basin-ejecta formations, and their definition is the same as previous studies (Wilhelms et al., 1987; Baker et al., 2012). However, the peak-ring and basin-rim formations are disputed.

4.1.1. Peak-ring formations of impact basins

Following Pike and Spudis (1987) and Baker et al. (2011a, 2011b), we plot the peak-ring diameter versus the rim-crest diameter for the lunar peak-ring and proto-basins, and the intermediate-ring diameter versus the inner-ring diameter. We calculate a linear fit of $D_{rim} = 1.97 * D_{ring}$ ($R^2 = 0.817$, where R is the correlation coefficient, and D_{ring} and D_{rim} is the peak-ring and basin rim-crest diameter, respectively) for the lunar peak-ring basins (Fig. 6a). The ratio of rim-crest and peak-ring diameter is ~ 2 , consistent with previous results (Head, 1977; Pike and Spudis, 1987; Baker et al., 2011a, 2011b). A basin deviates from the

trend substantially when the rim diameter is above 450 km with a larger ratio, such as the Fitzgerald-Jackson Basin (rim diameter = 625 km, peak-ring diameter = 359 km), Flamsteed-Billy Basin (rim diameter = 580 km, peak-ring diameter = 399 km) and Cruger-Sirsalis Basin (rim diameter = 549 km, peak-ring diameter = 341 km). It is interesting to find that all these three basins are of Aitkenian with a larger diameter, smaller ratio compared with other peak ring basins, and are distributed in or adjacent to high-Th areas and mid-latitudes of the Moon. The formation of these three Aitkenian basins may be different from other basins because of the influx of basalt after the impact event or the hot environment when the impact occurred (Melosh et al., 2017). The subsequent collapse of the transient crater, and the consequent modifications in crustal structure, depend sensitively on the shear strength of the crust and upper mantle, which is a strong function of temperature. The collapse of the transient crater on the warmer and weaker nearside is more extensive, which prevents the thickened crust surrounding the transient crater from collapsing back into the crater (Miljković et al., 2013), which resulted in a smaller ratio. The Moon is hotter in Aitkenian than in the other two periods, and the basin radius is larger in a warm target than in a cold one with the same given impact energy (Zhu et al., 2017), so these three basins are larger than others.

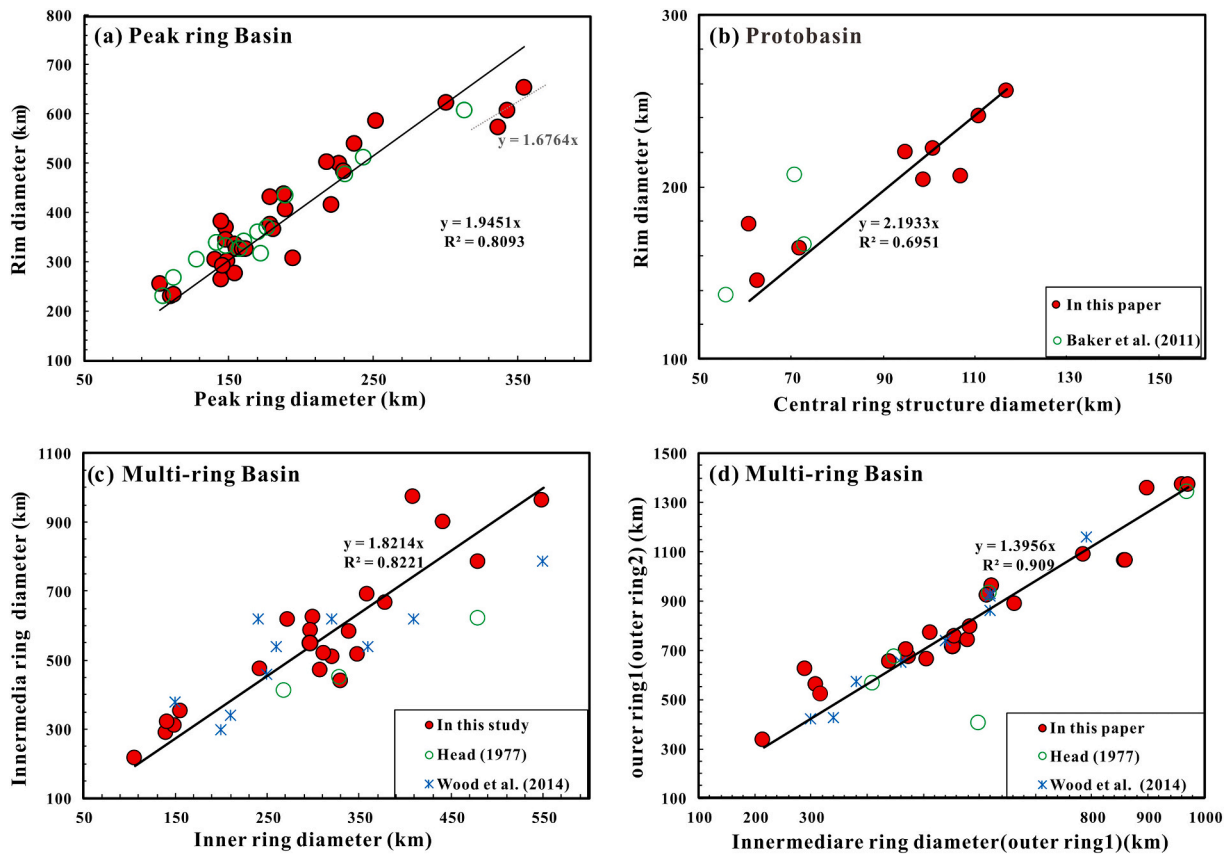


Fig. 7. PAN (Black solid points with red boundaries) with basins. (a) Compton basin; (b) Nectaris Basin; (c) Schrödinger Basin. (For interpretation of the references to colour in this figure legend, the reader is referred to the web version of this article.)

The linear fit for proto-basins is $D_{rim} = 2.19 \cdot D_{ring}$ ($R^2 = 0.695$) (Fig. 6b), similar to the published results (Baker et al., 2011a, 2011b). Meanwhile, the linear fit can be expressed as $D_{intermediate} = 1.82 \cdot D_{inner}$ ($R^2 = 0.822$) for multi-ring basins (where $D_{intermediate}$ and D_{inner} is the intermediate-ring and inner-ring diameter, respectively) (Fig. 6c). The results indicate that in terms of morphology, the central-ring structure in the proto-basins and the inner ring in the multi-ring basins is likely the peak-ring in the peak-ring basins.

Yamamoto et al. (2012) divided 134 the PAN exposure locations into 23 impact basins and 26 large craters using the Spectral Profiler onboard

the Japanese Kaguya lunar orbiter. All PAN sites are associated with huge impact structures with diameters larger than 100 km. On a localized scale, all regions with multiple PAN points are associated with small fresh craters or the slopes of peaks. Integrating our identification results with the PAN locations, most PAN appears in the peak-ring and peak formations of peak-ring and proto-basins (e.g., Schrödinger, Compton and Antoniadi basins) (Fig. 7a, c). Meanwhile, we found some PAN in the inter-ring geological units in many multi-ring basins (e.g., Crisium, Nectaris, and Orientale basins)(Fig. 7b) but not in other sub-formations (those found are mainly located in the peak or crater wall). These

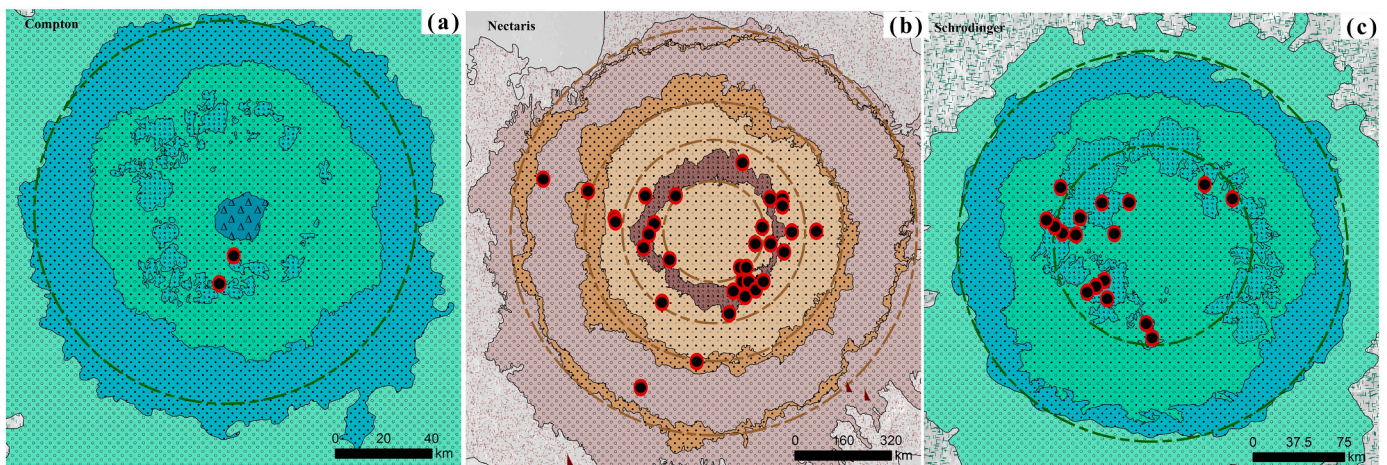


Fig. 8. Radial rim facies in the Orientale Basin. (a) The ideal rings (black rings) and actual layer (red regions) on LROC WAC image; (b) Radial facies (white arrows) in the intermediate ring in GRAIL Gradient; (c) Orientale basin's rings layer with LOLA DEM at 55% transparency overlaid on LROC WAC image; (d) Radial facies (white arrows) in the intermediate ring in LROC WAC image; (e) Radial rim facies (white arrows) in the intermediate ring in LROC WAC image. (For interpretation of the references to colour in this figure legend, the reader is referred to the web version of this article.)

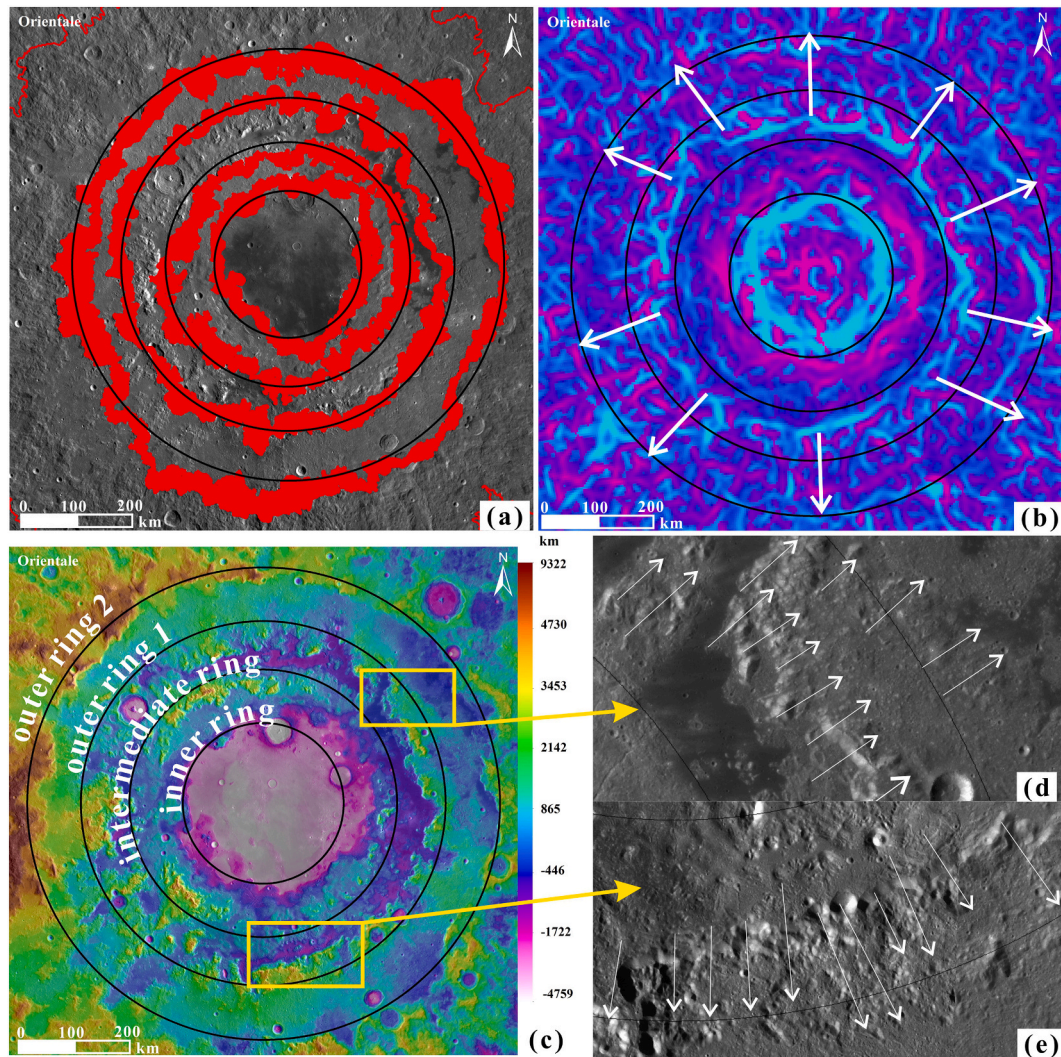


Fig. 9. Orientale Southwest Basin. (a) Orientale Southwest Basin's rings (white line) and edges (red line). The base map is composed of LOLA DEM slope data with 50% transparency, GRGM900 data with 60% transparency, Focal Flow spatial analysis data; (b) Orientale Southwest Basin's rings and edges. The base map is composed of GRGM900 data with 20% transparency, and Focal Flow spatial analysis; (c) The geologic map of Orientale Southwest Basin in this paper; (d) The background geologic map of Orientale Southwest Basin. (For interpretation of the references to colour in this figure legend, the reader is referred to the web version of this article.)

predictions on stratigraphic uplift are consistent with the abundance of PAN, which indicated the mechanisms of the central-ring structure in the proto-basins and the intermediate ring in the multi-ring basins are similar to the peak-ring in the peak-ring basins, they can all be named peak rings. These peak rings should come from the relatively shallow crust, controlled by the geometry of the excavation and melting cavities. Peak rings are envisioned to form through a combination of the complex, centrosymmetric, rotational collapse of the transient crater's walls and convergence of this collapse with the extreme uplifts of the crust and mantle that occur in the center of the basin (Baker et al., 2016).

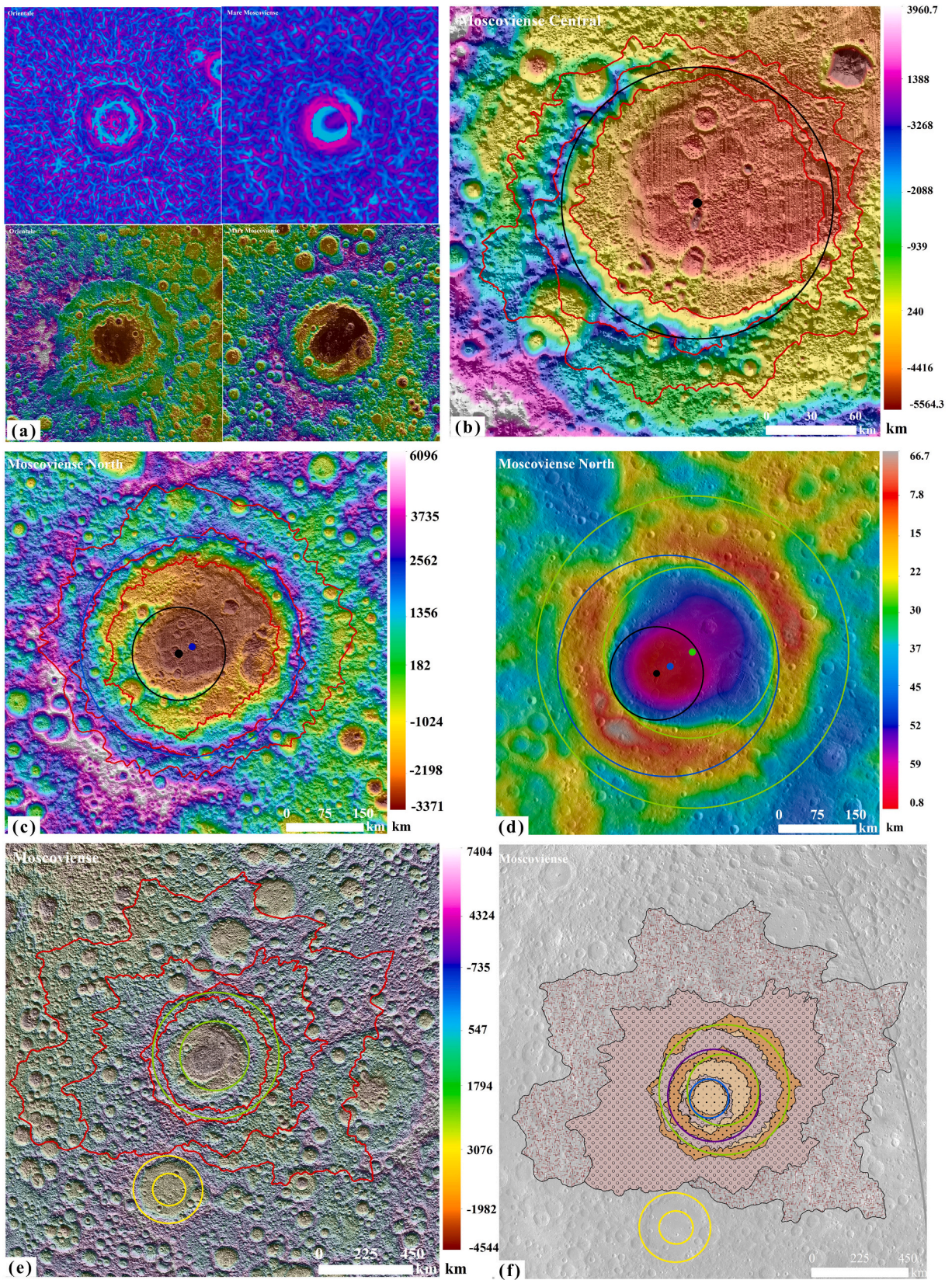
Consequently, we suggest that the inner rings in the multi-ring basins and the central-ring structure of the proto-basins have the same formation mechanism as the peak ring in peak-ring basins. Therefore, the sub-formations of the inner ring in the multi-ring basins and the central-ring structures of the proto-basins are divided as the peak-ring formation.

4.1.2. Rim formations of impact basins

There are some radial features outside the intermediate rings in multi-ring basins, which can be detected in both LROC WAC images and gravity gradients. As shown in Fig. 8, the radial facies can be traced to the intermediate ring (Outer Rook Ring) in the Orientale Basin, which

has been found by Head (1977). But there is no direct correlation between the radial facies with the distal ejecta blanket (Morse et al., 2018). Through numerical simulation, Johnson et al. (2016) suggested these radial facies are the result of the inward flow of warm, weak mantle material during the collapse of the transient crater. This flow of underlying weaker material pulls the cooler crust along with it, ultimately causing extensional faulting with large offsets far from the transient crater rim. Therefore, the materials of intermediate- and outer rings in multi-ring basins are related to the outer of the transient crater. Thus, the flat and radial areas in the intermediate- and outer rings in multi-ring basins are named by basin-rim formations, and the wall formations represent steep terrains.

The diameter ratio of the adjacent rings of multi-ring basins is a constant ($\sqrt{2}$; Hartmann and Kuiper, 1962; Spudis, 1993; Head 3rd et al., 2010; Johnson et al., 2018). In this study, the intermediate-ring diameter versus the inner-ring diameter of the multi-ring basins are close to 1.82 (Fig. 6c), The proportion of other adjacent rings except the inner ring conforms to the $\sqrt{2}$ (Fig. 6d). Accordingly, we speculate the $\sqrt{2}$ ring diameter ratio in the multi-ring basins may be related to the shock wave impact on the ejecta distribution, which verifies the numerical simulation results of Head 3rd et al. (2010). The collapse of the



(caption on next page)

Fig. 10. Moscovinies Basin. (a) Mare Moscoviense compared with Orientale Basin in gravity gradient data and DEM data; (b) Moscoviense Central Basin (LOLA DEM data with 90% transparency and Focal Flow spatial analysis data), the black spot is the center coordinates of Moscoviense Central Basin, the black ring is the ring of Moscoviense Central Basin, the red lines are the basin formation edge of Moscoviense Central Basin. In the northeast of the basin, the edge can not be identified in DEM data but it has a certain topographical fluctuation in Focal Flow spatial analysis data; (c) Moscoviense North Basin (LOLA DEM data with 90% transparency and Focal Flow spatial analysis data), the blue spot is the center coordinates of Moscoviense North Basin, the blue ring is the ring of Moscoviense North Basin, the red lines are the basin formation edge of Moscoviense North Basin; (d) Ring of Moscoviense Basin in GRAIL thickness, the green spot is the center of Moscoviense Basin, the green circle is the ring of Moscoviense Central Basin; (e) Formations of Moscoviense Basin (LOLA DEM data with 10% transparency and Focal Flow spatial analysis data), the green circle is the ring of Moscoviense Basin, the red lines are the basin formation edge of Moscoviense Basin. The inner basin formation topographical fluctuation and the outer radial ejecta texture are highlighted in Focal Flow spatial analysis data; (f) Merge formations of three basins in Mare Moscoviense. (For interpretation of the references to colour in this figure legend, the reader is referred to the web version of this article.)

rim likely forms a mega terrace, modifying the innermost radial ejecta on the basin rim to the observed domical facies.

4.2. Formation identification with special basins

4.2.1. Boundary recognition for severely-degraded basins

The severely-degraded basins have blurred morphological boundaries, and their detailed geological features are impossible to identify with a single set of lunar remote sensing data. Although the Orientale Southwest Basin was vaguely revealed by topography and GRAIL Bouguer gravity anomaly (Head 3rd et al., 2010; Neumann et al., 2015), detailed identification works are still lacking. Nearly all the sub-formations of the Orientale Southwest Basin are all covered by ejecta blankets and are hardly picked-up in LROC WAC images and LOLA DEM data, but some geologic information can be displayed in slope data, GRGM900 data, Focal Flow spatial analysis data, and shade hill data (Fig. S6).

Nearly all the sub-formations of the Orientale Southwest Basin are all covered by ejecta blankets and are hardly picked up in LROC WAC images and LOLA DEM data, but some geologic information can be displayed in slope data, GRGM900 data, Focal Flow spatial analysis data, and shade hill data (Fig. S6). In Fig. S6a, two inner peaks can be identified, but the other larger peak and outer basin formations are not obvious in the LROC WAC image. In Fig. S6b, three inner peaks and the boundary between the basin wall and the basin floor can be identified, but other basin formations are not obvious in shade hill data. In Fig. S6c, two inner peaks and the radial ejecta can be identified, but the other basin formations are not obvious in LOLA DEM slope data. In Fig. S6d, the boundary of gravity is faintly visible in GRGM900 data. In Fig. S6e, the basin formations are not obvious in LOLA DEM data. In Fig. S6f, Three inner peaks, the boundary of the basin wall and the basin floor, are all obvious, but the radial ejecta in the southwest is not well displayed. However, the radial ejecta grooves are faintly revealed in Focal Flow spatial analysis data. In summary, the focus stream can identify more comprehensive information than other data. Fusion with other data will be more conducive to the identification of the geological boundary of the basin.

We distinguished the geological structures (Fig. 9a-b) and certain impact characteristics. Three inner peaks, the basin wall, the basin floor are all obvious, and the radii ejecta in the southwest are well displayed (red lines in Fig. 8a). The ring structure of Orientale Southwest Basin can be found in the multi-data (GRGM900 data and Focal Flow spatial analysis data) (Fig. 8b). Based on these structures, we generated a geologic map for the Orientale Southwest basin (Fig. 9c). When merging the three-period basin sub-formations maps into a global map (Fig. 5a), the sub-formations of the Orientale Southwest basin are covered by Orientale Basin formations (Fig. 9d).

Basins which are partially degraded, such as the Serenitatis Basin (western part covered by the Imbrium Basin), Nubium Basin (southern part filled with basalts), Werner-Airy Basin (eastern part Overlapped with the Nectaris Basin), and the Medii Basin (northwestern part filled with basalts) are mapped similarly (Fig. 4).

4.2.2. Boundary recognition for basins with special formation mechanisms

The Mare Moscoviense shows unique characteristics not only in

terms of geology and mineralogy but also in geophysics (Fig. 10a). Based on the three-ring structures with the inconsistent center in Mare Moscoviense, there are two possible formation mechanisms (oblique impact or multiple impacts) (Ishihara et al., 2011; Thaisen et al., 2011; Byrne, 2016). In this study, we discovered a new ring (the green inner ring) based on the crustal thickness data (Wieczorek et al., 2013) and LOLA DEM (Fig. 10d), which is concentric with the outermost ring structure (the green outer ring) of the three known ring structures. The diametric ratio of the outermost ring and this new concentric ring is 2, consistent with the peak-ring formation law (Baker et al., 2011a, 2011b). In other words, this new ring is the peak ring of the Moscoviense Basin. These rings cross each other if the Mare Moscoviense is formed by an oblique impact event (Fig. 10d). Unfortunately, these rings intersect twice (a. the black ring and the inner green ring; b. the inner green ring and blue ring). More importantly, we have identified three independent ejecta around the black ring, the blue ring, and the outer green ring (Fig. 10b, c, e), which were formed by three impacts. Thus, we concluded that the Mare Moscoviense was formed by three basin-scale impact events. The three impact events (from old to young) are also recorded in the Moscoviense Basin, Moscoviense North Basin, Moscoviense Central Basin (Byrne, 2016) (Fig. 10). Thus, we concluded that the Mare Moscoviense was formed by three basin-scale impact events. The three impact events (from old to young) are also recorded in the Moscoviense Basin, Moscoviense North Basin, Moscoviense Central Basin (Byrne, 2016) (Fig. 10).

Detailed geologic sub-formations in the Mare Moscoviense are shown in Fig. 10. We classified the Moscoviense Central Basin and Moscoviense North Basin as proto-basins, and mapped their rings and edges using the LOLA and LROC WAC data (Fig. 10b-c). The Moscoviense Basin is regarded as a peak-ring basin using the GRAIL crustal thickness data (Fig. 10d). In this study, mapping of the basins was confined to the rim and basin-floor formations due to the limited GRAIL data resolution (Fig. 10e). The regional map was generated by combining the sub-formations of the three basins (Fig. 10f). Combining the oblique impact mechanism (Melosh, 1989) with the central coordinate of the three basins (Fig. 10d) and the rim formation distribution (Fig. 10a-e), The three impact bodies may be one impact body split and the impact direction is SW-NS (Fig. 10f). We purposed that the ejecta distribution in southwestern Mare Moscoviense has been disturbed by later impact events and filled by later basalts.

4.2.3. South Pole-Aitken (SPA) basin

The SPA is the largest and oldest preserved impact basin in the solar system (Evans et al., 2018). The structure is large enough to be classified as one of the three significant terranes (The Procellarum KREEP Terrane, the Felspathic Highlands Terrane, and the South Pole-Aitken Terrane) (Jolliff et al., 2000). The geology and structure of SPA have been studied by many scholars, such as the structure of the SPA basin outer ring (Shevchenko et al., 2007; Garrick-Bethell and Zuber, 2009), the mineralogical maps of the SPA basin (Ohtake et al., 2014; Moriarty and Pieters, 2018), the mare basalt or volcanism in or around the SPA (Pieters et al., 2001; Pasckert et al., 2018a, 2018b), the ejecta contribution (Melosh et al., 2017; Moriarty et al., 2021). However, the impact basin sub-formations of the SPA have not been well studied owing to the serious degradation by later basin impact events (Wilhelms et al., 1987).

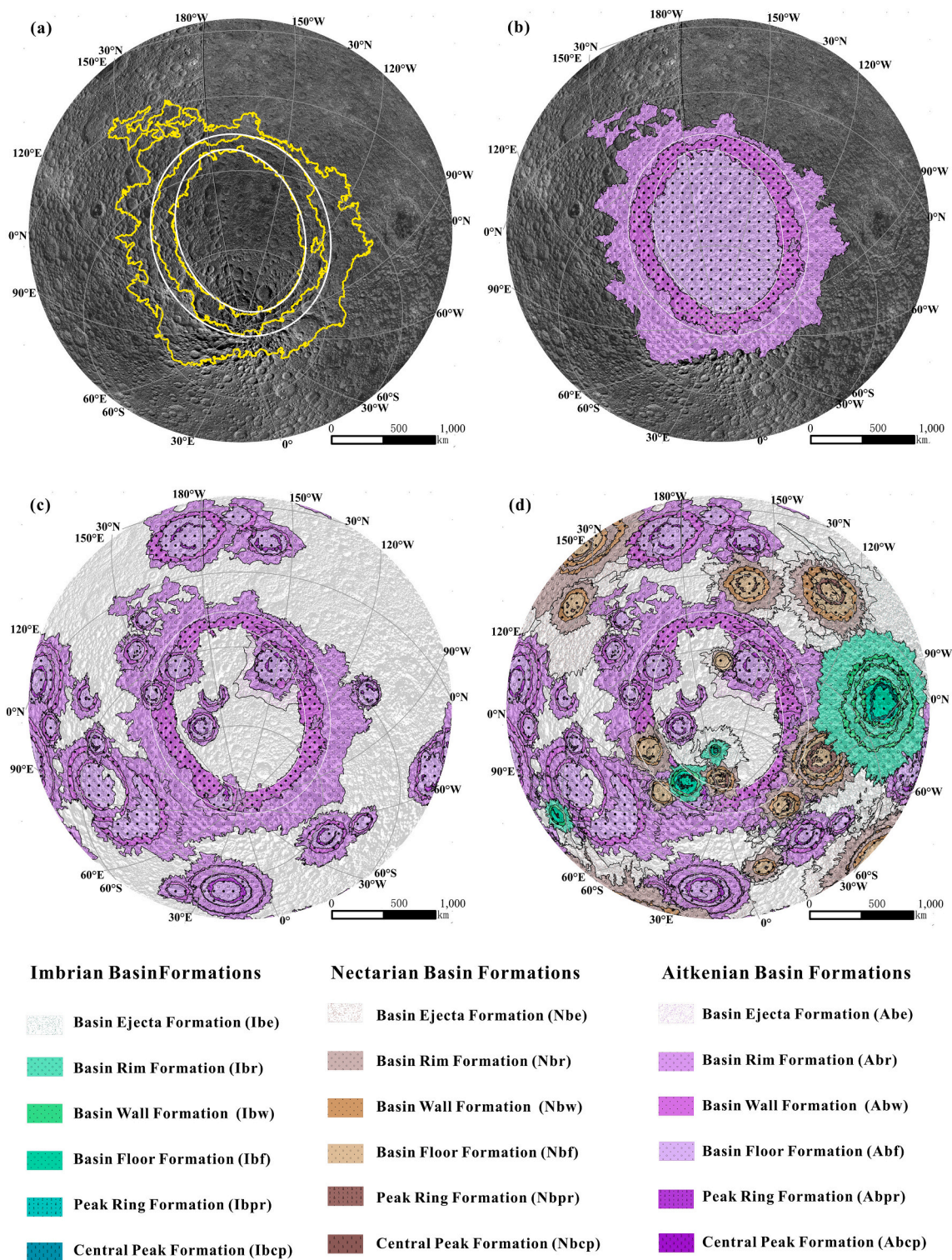


Fig. 11. The sub-formations of SPA (a) edge of SPA's formations, yellow lines are the edges of the SPA basin formations, the white line is the ring Of SPA; (b) SPA's formations; (c) Aitkenian-aged basins' formations in SPA area; (d) Three-period basins formations in the SPA area. The polar coordinate projection is used by these 4 subgraphs, the Projection is Lambert Azimuthal Equal Area (Central_Meridian: -177.8, Latitude_Of_Origin: -56.0). (For interpretation of the references to colour in this figure legend, the reader is referred to the web version of this article.)

Based on its topography, FeO and TiO₂ signatures, and its elliptical structure lines (Garrick-Bethell and Zuber, 2009), we have mapped the basin-floor, basin-wall, and rim formations of the SPA (Fig. 11 a-b). Previous studies indicate that the northeastern SPA (higher terrain and thicker lunar crust than other SPA surroundings) was formed from the impact ejecta of SPA (Melosh et al., 2017), yet there are no continuous

SPA radial sub-formations revealed from the elevation trends, element distributions, or gravity features. We purposed that the higher terrain and thicker lunar crust is a result of five younger basin impact events (Orientale, Orientale Southwest, Hertzprung, Dirichlet-Jackson, and Korolov) in the northeastern SPA (Fig. 11d), or the original terrain was higher than the surrounding terrains before the impact happened.

Moreover, we recognized more rim formations in the northwestern SPA, which may indicate the impact direction at SPA was SE-NW. This map is consistent with the hypsometric map and the basin height profiles of SPA (Garrick-Bethell and Zuber, 2009), but the ejecta are not well identified as the result of the numerical simulation (Melosh et al., 2017; Moriarty et al., 2021) as the degradation of SPA.

4.3. Potential applications in future

Impact basins were formed during 700 Ma in the early lunar history, during which the Moon had also experienced rapid thermal evolution (Zhu et al., 2017), the Moon was thought to be much hotter 4.5 Ga ago and cooled significantly over the next 700 Ma (Laneuville et al., 2013). The possible basin impact conditions (incl. Impact angle, velocity, and direction) (Melosh, 1989) can be obtained by analyzing the basin sub-formation characteristics. Furthermore, these impact conditions can provide some clues for exploring the source of the late heavy bombardment (LHB) (Bottke and Norman, 2017). The basin degradation degree combined with the basin sub-formations can get the impact sequence of impact basins (Fassett et al., 2012). The mascon size combined with the basin sub-formations can reveal the early lunar thermal evolution (Miljković et al., 2013), and the rock distributions (e.g., basalt and PAN) and element distributions (e.g., FeO and TiO₂) combined with the basin sub-formations can provide clues for the basin impact mechanism (Spudis, 1993).

Mineral characteristics, topography, and deep structures are all emplaced by basin-scale impact events on the Moon. The basin sub-formation map can contribute to facilitating future lunar exploration. For example, the Chinese spacecraft Chang'E-4 landed in the Von Kármán crater inside the SPA basin (Li et al., 2019). Our results show that the landing site is at the floor formation of the SPA and Von Kármán M basins. The geologic characteristics are influenced by the ejecta formation of the Ingenii and Poincaré basins (Fig. s7). The basin sub-formation map can provide important information to refine the geological characteristics and evolution of the Chang'E-4 region.

5. Conclusions

Integrating remote sensing interpretation with the basin-scale impact formation mechanism, we established a list of features for basin identification and produced a new lunar basin catalog that contains 81 basins, including 24 proto-basins, 32 peak-ring basins, 24 multi-ring basins, and one super basin. According to the ring diameter ratios, PAN distribution, and basin radial textures, the basin sub-formations are divided into six types, i.e., central peak, peak-ring, basin-floor, basin-wall, basin-rim, and basin-ejecta formations. The new lunar geologic map in this paper shows a more precise distribution of basin formations, covering nearly 70% of the lunar surface. To draw a more comprehensive geological map of the basin, the basin sub-formations of severely degraded basins and special basins are identified (for example Orientale Southwest Basin, SPA), the impact mechanism of the Mare Moscoviense are elaborated. The new map can contribute to our understanding of the origin of basin rings, impact conditions, lunar thermal history, as well as the geological characteristics and evolution of lunar exploration sites.

Data availability

LOLA, LROC WAC, GRAIL900C: <https://pds-geosciences.wustl.edu/dataserv/moon.html>
 or <https://astrogeology.usgs.gov/search?pmi-target=moon>
 GRAILCrustalThickness: <http://www.ipgp.fr/~wieczor/GRAILCrustalThicknessArchive/GRAILCrustalThicknessArchive.html>
 Gradients of the gravity data: <https://data.mendeley.com/datasets/pz874f2bs2/>
 Chang'E data <http://202.106.152.98:8081/moondata/>

Declaration of Competing Interest

The authors declare that they have no known competing financial interests or personal relationships that could have influenced the work reported in this paper.

Acknowledgments

We are grateful for comments on earlier versions of this paper from ***reviewers. We gratefully acknowledge Professor Zongcheng Ling and Dr. Jian Chen from Shandong University to distribute PAN analysis. We would like to thank Professor Xiaozhong Ding and Dr. Kejuan Xu from the Chinese Academy of Geological Sciences for their assistance during the legend design of impact basin formations. This study was funded by the Strategic Priority Research Program (B) of the Chinese Academy of Sciences (Grant No. XDB 41000000 and No. XDB18000000), the National Key Basic Research Special Foundation of China (Grant No. 2015FY210500), Beijing Municipal Science and Technology Commission (Grant No. Z181100002918003), the Chinese Academy of Sciences Interdisciplinary Innovation Team, the Key Program of Frontier Science of Chinese Academy of Sciences (Grant No. QYZDY-SSW-DQC028), and the National Natural Science Foundation of China (Grant No. 41773065 and No. 41941003).

Appendix A. Supplementary data

Supplementary data to this article can be found online at <https://doi.org/10.1016/j.icarus.2022.114952>.

References

- Alexopoulos, J.S., McKinnon, W.B., 1994. Large impact craters and basins on Venus, with implications for ring mechanics on the terrestrial planets. In: *Large Meteorite Impacts and Planetary Evolution. Special Papers-geological Society of America*, pp. 29–45.
- Andrews-Hanna, J.C., Head, J.W., Johnson, B., Keane, J.T., Kiefer, W.S., McGovern, P.J., Neumann, G.A., Wieczorek, M.A., Zuber, M.T., 2018. Ring faults and ring dikes around the Orientale basin on the Moon. *Icarus* 310, 1–20. <https://doi.org/10.1016/j.icarus.2017.12.012>.
- Baker, D.M.H., Head, J.W., Schon, S.C., Ernst, C.M., Prockter, L.M., Murchie, S.L., Denevi, B.W., Solomon, S.C., Strom, R.G., 2011a. The transition from complex crater to peak-ring basin on Mercury: New observations from MESSENGER flyby data and constraints on basin formation models. *Planet. Space Sci.* 59 (15), 1932–1948. <https://doi.org/10.1016/j.pss.2011.05.010>.
- Baker, D.M.H., Head, J.W., Collins, G.S., Potter, R.W.K., 2016. The formation of peak-ring basins: working hypotheses and path forward in using observations to constrain models of impact-basin formation. *Icarus* 273, 146–163. <https://doi.org/10.1016/j.icarus.2015.11.033>.
- Baker, D.M.H., Head, J.W., Fassett, C.I., Kadish, S.J., Smith, D.E., Zuber, M.T., Neumann, G.A., 2011b. The transition from complex crater to peak-ring basin on the Moon: New observations from the Lunar Orbiter Laser Altimeter (LOLA) instrument. *Icarus* 214 (2), 377–393. <https://doi.org/10.1016/j.icarus.2011.05.030>.
- Baker, D.M., Head, J.W., Neumann, G.A., Smith, D.E., Zuber, M.T., 2012. The transition from complex craters to multi-ring basins on the Moon: Quantitative geometric properties from Lunar Reconnaissance Orbiter Lunar Orbiter Laser Altimeter (LOLA) data. *J. Geophys. Res. Planets* 117, E12. <https://doi.org/10.1029/2011je004021>.
- Baker, D.M.H., Head, J.W., Phillips, R.J., Neumann, G.A., Bierson, C.J., Smith, D.E., Zuber, M.T., 2017. GRAIL gravity observations of the transition from complex crater to peak-ring basin on the Moon: Implications for crustal structure and impact basin formation. *Icarus* 292, 54–73. <https://doi.org/10.1016/j.icarus.2017.03.024>.
- Bottke, W.F., Norman, M.D., 2017. The Late Heavy Bombardment. *Annu. Rev. Earth Planet. Sci.* 45 (1), 619–647. <https://doi.org/10.1146/annurev-earth-063016-020131>.
- Byrne, C.J., 2016. *The Moon's Largest Craters and Basins*. Springer International Publishing.
- Chen, J.P., Xu, Y.B., Wang, X., He, S.J., Yan, D.P., Liu, S.F., Zou, Y.L., Zheng, Y.C., 2014. Geotectonic evolution of lunar LQ-4 region based on multisource data. *Geosci. Front.* 5 (2), 227–235. <https://doi.org/10.1016/j.gsf.2013.05.006>.
- Conrad, J.W., Nimmo, F., Fassett, C.I., Kamata, S., 2018. Lunar impact history constrained by GRAIL-derived basin relaxation measurements. *Icarus* 314, 50–63. <https://doi.org/10.1016/j.icarus.2018.05.029>.
- Evans, A.J., Andrews-Hanna, J.C., Head, J.W., Soderblom, J.M., Solomon, S.C., Zuber, M.T., 2018. Reexamination of Early Lunar Chronology With GRAIL Data: Terranes, Basins, and Impact Fluxes. *J. Geophys. Res. Planets* 123 (7), 1596–1617. <https://doi.org/10.1029/2017je005421>.
- Fassett, C.I., Head, J.W., Smith, D.E., Zuber, M.T., Neumann, G.A., 2011. Thickness of proximal ejecta from the Orientale Basin from Lunar Orbiter Laser Altimeter (LOLA)

- data: Implications for multi-ring basin formation. *Geophys. Res. Lett.* 38, L17201. <https://doi.org/10.1029/2011gl048502>.
- Fassett, C.I., Head, J.W., Kadish, S.J., Mazarico, E., Neumann, G.A., Smith, D.E., Zuber, M.T., 2012. Lunar impact basins: Stratigraphy, sequence and ages from superposed impact crater populations measured from Lunar Orbiter Laser Altimeter (LOLA) data. *J. Geophys. Res. Planets* 117. <https://doi.org/10.1029/2011JE003951>.
- Fortezzo, C.M., Spudis, P.D., Harrel, S.L., 2020. Unified Geologic Map of the Moon, 1:5M, 2020. USGS Astrogeology Science Center. Astrogeology https://astrogeology.usgs.gov/search/map/Moon/Geology/Unified_Geologic_Map_of_the_Moon_GIS_v2.
- Garrick-Bethell, I., Zuber, M.T., 2009. Elliptical structure of the lunar South Pole-Aitken basin. *Icarus* 204 (2), 399–408. <https://doi.org/10.1016/j.icarus.2009.05.032>.
- Guo, D., Liu, J., Zhang, L., Ji, J., Liu, J., Wang, L., 2014. The methods of lunar geochronology study and the subdivisions of lunar geologic history. *Geosci. Front.* 21 (6), 45–61. <https://doi.org/10.13745/j.esf.2014.06.006>.
- Hartmann, W.K., Kuiper, G.P., 1962. Concentric Structures Surrounding Lunar Basins. *Communicat. Lunar Planet. Lab.* 1, 51–66.
- Hartmann, W.K., Wood, C.A., 1971. Moon: Origin and evolution of multi-ring basins: The Moon 3, 1, 3–78. <https://doi.org/10.1007/bf00620390>.
- Hawke, B., Head, J., 1977. Impact melt on lunar crater rims. In: *Proceedings Impact and explosion cratering: Planetary and terrestrial implications*, pp. 815–841.
- Head, J.W., 1977. Origin of central peaks and peak rings - evidence from peak-ring basins on moon, mars, and mercury. *Trans. Am. Geophys. Union* 58 (6), 485–487.
- Head 3rd, J.W., Fassett, C.I., Kadish, S.J., Smith, D.E., Zuber, M.T., Neumann, G.A., Mazarico, E., 2010. Global distribution of large lunar craters: implications for resurfacing and impactor populations. *Science* 329, 1504–1507. <https://doi.org/10.1126/science.1195050>.
- Hiesinger, H., 2003. Ages and stratigraphy of mare basalts in Oceanus Procellarum, Mare Nubium, Mare Cognitum, and Mare Insularum. *J. Geophys. Res.* 108, E7. <https://doi.org/10.1029/2002je001985>.
- Hiesinger, H., Head, J., Wolf, U., Jaumann, R., Neukum, G., Advances, J.R., 2011. Ages and stratigraphy of lunar mare basalts: A synthesis. *Lunar Stratigr.* 477, 1–51. [https://doi.org/10.1130/2011.2477\(01\)](https://doi.org/10.1130/2011.2477(01)).
- Hodges, C.A., Wilhelms, D.E., 1978. Formation of lunar basin rings. *Icarus* 34, 294–323. [https://doi.org/10.1016/0019-1035\(78\)90169-0](https://doi.org/10.1016/0019-1035(78)90169-0).
- Ishihara, Y., Morota, T., Nakamura, R., Goossens, S., Sasaki, S., 2011. Anomalous Moscoviense basin: Single oblique impact or double impact origin? *Geophys. Res. Lett.* 38, L03201. <https://doi.org/10.1029/2010gl045887>.
- Ishihara, Y., Saruwatari, Y., Sawada, A., Morota, T., Hiramatsu, Y., 2014. Quantitative measurement method for impact basin characteristics based on localized spherical harmonics. *Icarus* 228, 315–323. <https://doi.org/10.1016/j.icarus.2013.10.018>.
- Johnson, B.C., Andrews-Hanna, J.C., Collins, G.S., Freed, A.M., Melosh, H.J., Zuber, M. T., 2018. Controls on the Formation of Lunar Multiring Basins. *J. Geophys. Res. Planets* 123, 3035–3050. <https://doi.org/10.1029/2018je005765>.
- Johnson, B.C., Blair, D.M., Collins, G.S., Melosh, H.J., Freed, A.M., Taylor, G.J., Head, J. W., Wiecezorek, M.A., Andrews-Hanna, J.C., Nimmo, F., Keane, J.T., Miljkovic, K., Soderblom, J.M., Zuber, M.T., 2016. Formation of the Orientale lunar multiring basin. *Science* 354 (6311), 441–444. <https://doi.org/10.1126/science.aag0518>.
- Jolliff, B.L., Gillis, J.J., Haskin, L.A., Korotev, R.L., Wiecezorek, M.A., 2000. Major lunar crustal terranes: Surface expressions and riel-mantle origins. *J. Geophys. Res. Planets* 105 (E2), 4197–4216. <https://doi.org/10.1029/1999je001103>.
- Laneville, M., Wiecezorek, M.A., Breuer, D., Tosi, N., 2013. Asymmetric thermal evolution of the Moon. *J. Geophys. Res. Planets* 118 (7), 1435–1452. <https://doi.org/10.1002/jgre.20103>.
- Le Feuvre, M., Wiecezorek, M.A., 2011. Nonuniform cratering of the Moon and a revised crater chronology of the inner Solar System. *Icarus* 214 (1), 1–20. <https://doi.org/10.1016/j.icarus.2011.03.010>.
- Li, C.L., Liu, D.W., Liu, B., Ren, X., Liu, J.J., He, Z.P., Zuo, W., Zeng, X.G., Xu, R., Tan, X., Zhang, X.X., Chen, W.L., Shu, R., Wen, W.B., Su, Y., Zhang, H.B., Ouyang, Z.Y., 2019. Chang'E-4 initial spectroscopic identification of lunar far-side mantle-derived materials. *Nature* 569 (7756), 378–382. <https://doi.org/10.1038/s41586-019-1189-0>.
- Losiak, A., Wilhelms, D.E., Byrne, C.J., Thaisen, K.G., Weider, S.Z., Kohout, T., O'Sullivan, K., Kring, D.A., Lunar Impact Crater Database. <https://www.lpi.usra.edu/lunar/surface/index.shtml#craters>.
- Lucey, P.G., Blewett, D.T., Hawke, B.R., 1998. Mapping the FeO and TiO₂ content of the lunar surface with multispectral imagery. *J. Geophys. Res. Planets* 103 (E2), 3679–3699. <https://doi.org/10.1029/97JE03019>.
- Melosh, H.J., 1989. *Impact cratering: A geologic process. Research supported by NASA, No. 11.* Oxford University Press (Oxford Monographs on Geology and Geophysics, New York), p. 253.
- Melosh, H.J., Kendall, J., Horgan, B., Johnson, B.C., Bowling, T., Lucey, P.G., Taylor, G. J., 2017. South Pole-Aitken basin ejecta reveal the Moon's upper mantle. *Geology* 45 (12), 1063–1066. <https://doi.org/10.1130/g39375.1>.
- Miljković, K., Wiecezorek, M.A., Collins, G.S., Laneville, M., Neumann, G.A., Melosh, H. J., Solomon, S.C., Phillips, R.J., Smith, D.E., Zuber, M.T., 2013. Asymmetric distribution of lunar impact basins caused by variations in target properties. *Science* 342 (6159), 724–726. <https://doi.org/10.1126/science.1243224>.
- Moriarty, D.P., Pieters, C.M., 2018. The character of south Pole-Aitken basin: patterns of surface and subsurface composition. *J. Geophys. Res. Planets* 123 (3), 729–747. <https://doi.org/10.1002/2017je005364>.
- Moriarty, D.P., Watkins, R.N., Valencia, S.N., Kendall, J.D., Evans, A.J., Dygert, N., Petro, N.E., 2021. Evidence for a stratified upper mantle preserved within the South Pole-Aitken Basin. *J. Geophys. Res. Planets* 126, 1. <https://doi.org/10.1029/2020je006589>.
- Morio, M., Finkel, M., Martac, E., 2010. Flow guided interpolation – A GIS-based method to represent contaminant concentration distributions in groundwater. *Environ. Model. Softw.* 25 (12), 1769–1780. <https://doi.org/10.1016/j.envsoft.2010.05.018>.
- Morse, Z.R., Osinski, G.R., Tornabene, L.L., 2018. New morphological mapping and interpretation of ejecta deposits from Orientale Basin on the Moon. *Icarus* 299, 253–271. <https://doi.org/10.1016/j.icarus.2017.08.010>.
- Neumann, G.A., Zuber, M.T., Wiecezorek, M.A., Head, J.W., Baker, D.M., Solomon, S.C., Smith, D.E., Lemoine, F.G., Mazarico, E., Sabaka, T.J., Goossens, S.J., Melosh, H.J., Phillips, R.J., Asmar, S.W., Konopliv, A.S., Williams, J.G., Sori, M.M., Soderblom, J. M., Miljkovic, K., Andrews-Hanna, J.C., Nimmo, F., Kiefer, W.S., 2015. Lunar impact basins revealed by Gravity Recovery and Interior Laboratory measurements. *Sci. Adv.* 1, E1500852. <https://doi.org/10.1126/sciadv.1500852>.
- Ohtake, M., Uemoto, K., Yokota, Y., Morota, T., Yamamoto, S., Nakamura, R., Haruyama, J., Iwata, T., Matsunaga, T., Ishihara, Y., 2014. Geologic structure generated by large-impact basin formation observed at the South Pole-Aitken basin on the Moon. *Geophys. Res. Lett.* 41 (8), 2738–2745. <https://doi.org/10.1002/2014GL059478>.
- Osinski, G.R., 2012. *Impact Cratering: Processes and Products*.
- Pasckert, J.H., Hiesinger, H., van der Bogert, C.H., 2018a. Lunar farside volcanism in and around the South Pole-Aitken basin. *Icarus* 299, 538–562. <https://doi.org/10.1016/j.icarus.2017.07.023>.
- Pasckert, J.H., Hiesinger, H., van der Bogert, C.H., 2018b. Lunar farside volcanism in and around the South Pole-Aitken basin. *Icarus* 299, 538–562. <https://doi.org/10.1016/j.icarus.2017.07.023>.
- Pieters, C.M., Staid, M.I., Fischer, E.M., Tompkins, S., He, G., 1994. A sharper view of impact craters from clementine data. *Science* 266 (5192), 1844–1848. <https://doi.org/10.1126/science.266.5192.1844>.
- Pieters, C.M., Head, J.W., Gaddis, L., Jolliff, B., Duke, M., 2001. Rock types of South Pole-Aitken basin and extent of basaltic volcanism. *J. Geophys. Res. Planets* 106 (E11), 28001–28022. <https://doi.org/10.1029/2000je001414>.
- Pike, R.J., Spudis, P.D., 1987. Basin-ring spacing on the moon, mercury, and mars. *Earth Moon Planet.* 39, 129–194. <https://doi.org/10.1007/Bf00054060>.
- Potter, R.W.K., 2015. Investigating the onset of multi-ring impact basin formation. *Icarus* 261, 91–99. <https://doi.org/10.1016/j.icarus.2015.08.009>.
- Potter, R.W.K., Head, J.W., Guo, D., Liu, J., Xiao, L., 2018. The Apollo peak-ring impact basin: Insights into the structure and evolution of the South Pole-Aitken basin. *Icarus* 306, 139–149. <https://doi.org/10.1016/j.icarus.2018.02.007>.
- Robinson, M.S., Brylow, S.M., Tschimmel, M., Humm, D., Lawrence, S.J., Thomas, P.C., Denevi, B.W., Bowman-Cisneros, E., Zerr, J., Ravine, 2010. Lunar Reconnaissance Orbiter Camera (LROC) instrument overview. *Space Sci. Rev.* 150 (1–4), 81–124. <https://doi.org/10.1007/s11214-010-9634-2>.
- Salvador, A., 1994. *International stratigraphic guide: a guide to stratigraphic classification, terminology, and procedure.* Geological Society of America.
- Schultz, P.H., Crawford, D.A., 2016. Origin and implications of non-radial Imbrium Sculpture on the Moon. *Nature* 535 (7612), 391–394. <https://doi.org/10.1038/nature18278>.
- Shevchenko, V.V., Chikmachev, V.I., Pugacheva, S.G., 2007. Structure of the South Pole-Aitken lunar basin. *Sol. Syst. Res.* 41 (6), 447–462. <https://doi.org/10.1134/s0038094607060019>.
- Sliz, M., Spudis, P.D., 2016. New Geological Map of the Lunar Crisium Basin. In: *47th Lunar and Planetary Science Conference. Abstract # 1678*.
- Smith, D.E., Zuber, M.T., Neumann, G.A., Lemoine, F.G., Mazarico, E., Torrence, M.H., McGarry, J.F., Rowlands, D.D., Head, J.W., Duxbury, T.H., Aharonson, O., Lucey, P. G., Robinson, M.S., Barnouin, O.S., Cavanaugh, J.F., Sun, X.L., Liiva, P., Mao, D.D., Smith, J.C., Bartels, A.E., 2010. Initial observations from the Lunar Orbiter Laser Altimeter (LOLA). *Geophys. Res. Lett.* 37, (18). <https://doi.org/10.1029/2010gl043751>.
- Spudis, P.D., 1993. *The Geology of Multi-ring Impact Basins.* Cambridge University, p. 277.
- Spudis, P.D., Martin, D.J.P., Kramer, G., 2014. Geology and composition of the Orientale Basin impact melt sheet. *J. Geophys. Res. Planets* 119 (1), 19–29. <https://doi.org/10.1002/2013je004521>.
- Steenstra, E.S., Martin, D.J.P., McDonald, F.E., Paisarnsombat, S., Kring, D.A., 2016. Analyses of robotic traverses and sample sites in the Schrödinger basin for the HERACLES human-assisted sample return mission concept. *Adv. Space Res.* 58 (6), 1050–1065. <https://doi.org/10.1016/j.asr.2016.05.041>.
- Thaisen, K.G., Head, J.W., Taylor, L.A., Kramer, G.Y., Isaacson, P., Nettles, J., Petro, N., Pieters, C.M., 2011. Geology of the Moscoviense Basin. *J. Geophys. Res.* 116. <https://doi.org/10.1029/2010je003732>.
- Wiecezorek, M.A., Neumann, G.A., Nimmo, F., Kiefer, W.S., Taylor, G.J., Melosh, H.J., Phillips, R.J., Solomon, S.C., Andrews-Hanna, J.C., Asmar, S.W., Konopliv, A.S., Lemoine, F.G., Smith, D.E., Watkins, M.M., Williams, J.G., Zuber, M.T., 2013. The Crust of the Moon as Seen by GRAIL. *Science* 339 (6120), 671–675. <https://doi.org/10.1126/science.1231530>.
- Wilhelms, D.E., John, F., Trask, N.J., 1987. *The Geologic History of the Moon*, pp. 2330–7102.
- Wood, C.A., 2004. Impact Basin Database [online] available at <http://www.lpod.org/cw/DataStuff/Lunar%20Basins.htm>.
- Wu, Y., Li, L., Luo, X., Lu, Y., Chen, Y., Pieters, C.M., Basilevsky, A.T., Head, J.W., 2018. Geology, tectonism and composition of the northwest Imbrium region. *Icarus* 303, 67–90. <https://doi.org/10.1016/j.icarus.2017.12.029>.
- Yamamoto, S., Nakamura, R., Matsunaga, T., Ogawa, Y., Ishihara, Y., Morota, T., Hirata, N., Ohtake, M., Hiroi, T., Yokota, Y., Haruyama, J., 2012. Massive layer of

- pure anorthosite on the Moon. *Geophys. Res. Lett.* 39 (13) <https://doi.org/10.1029/2012gl052098>.
- Zhu, M.H., Wünnemann, K., Artemieva, N., 2017. Effects of Moon's thermal state on the impact basin ejecta distribution. *Geophys. Res. Lett.* 44, 22, 11292–211300. <https://doi.org/10.1002/2017GL075405>.
- Zuber, M.T., Smith, D.E., Watkins, M.M., Asmar, S.W., Konopliv, A.S., Lemoine, F.G., Melosh, H.J., Neumann, G.A., Phillips, R.J., Solomon, S.C., Wieczorek, M.A., Williams, J.G., Goossens, S.J., Kruizinga, G., Mazarico, E., Park, R.S., Yuan, D.N., 2013. Gravity field of the Moon from the Gravity Recovery and Interior Laboratory (GRAIL) mission. *Science* 339, 668–671. <https://doi.org/10.1126/science.1231507>.